University of Alberta

Regional reflectivity analyses of the upper mantle using SS precursors and receiver functions

by

Sean M. Contenti

A thesis submitted to the Faculty of Graduate Studies and Research
in partial fulfillment of the requirements for the degree of

Master of Science
in
Geophysics

Department of Physics

Abstract

SS precursor imaging and receiver function analysis allow for a detailed investigation of mantle structure of the Earth and subduction dynamics due to their sensitivities to the sharp velocity contrasts within the mantle. By investigating the lateral depth variability of mantle seismic interfaces, primarily the *410* and *660*, this thesis explores the mantle structure beneath South and North America. In South America, we utilize over 5000 *SS* precursor waveforms to investigate the high–resolution reflectivity structure of the upper 1200 km of the mantle. In the vicinity of the subducting Nazca slab we observe a ∼1500–km wide reflection gap on the *410*, significant variability of the *660*, and scattered lower mantle reflections. These observations support the existence of a slab–related compositional heterogeneity atop the *410*, significant slab deformation with the transition zone, and combined Nazca slab stagnation and penetration at the base of the upper mantle. In North America, we compute over 1800 P–to–s receiver functions to investigate the local structure of the mantle beneath Alberta. We observe correlated depression of the *410* and *660* consistent strong upper mantle heterogeneity. Thickened transition zone and increased P wave velocities in southernmost Alberta are potentially associated with a remnant of the Farallon-Kula plate near the base of the upper mantle.

Acknowledgements

I would like to thank everyone who helped me throughout the completion of this thesis. Firstly, my supervisors, Jeff Gu and Mauricio Sacchi, for their invaluable assistance and mentoring throughout my time at the University. I would like to thank my fellow graduate students, Ahmet Okeler, Dave Bonar, Ryan Schultz, and Luyi Shen.

Lastly, I would like to thank my wife, Megan, for her unending support and encouragement.

Table of Contents

List of Tables

List of Figures

List of Symbols and Abbreviations

410   410-km Discontinuity

660   660-km Discontinuity

CANOE Canadian North-West Experiment

CMP   Common Mid-point

CNSN   Canadian National Seismograph Network

CRANE Canadian Rockies and Alberta Network

IRIS   Incorporated Research Institutions for Seismology

MTZ   Mantle Transition Zone

PREM   Preliminary Reference Earth Model

PRT   Parabolic Radon Transform

RF   Receiver function

RUM   Regionalized Upper Mantle

SAREX Southern Alberta Refraction Experiment

SNORCLE Slave & Northern Cordillera Lithospheric Evolution

SNR   Signal-to-Noise Ratio

SSA   Singular Spectrum Analysis

SVD   Singular Value Decomposition

THO   Trans-Hudson Orogen

WCSB   Western Canadian Sedimentary Basin

CHAPTER 1

Introduction

The large–scale interior structure of the Earth is among the oldest topics of research in modern seismology, beginning with the discovery of the liquid outer core [*Ben-Menaham*, 1995; *Oldham*, 1906] and the boundary between the crust and mantle [*Ben-Menaham*, 1995; *Mohorovicic*, 1909]. Research continued with the identification of the solid inner core [*Ben-Menaham*, 1995; *Lehmann*, 1936], and the identification of a transition region between the upper and lower mantle consisting of a high velocity gradient zone from 400–1000 km depth [*Bullen*, 1956]. The boundaries of the transition zone were later refined by seismic observations of discontinuous velocity increases at 410 and 660 km, and this region was termed the Mantle Transition Zone (MTZ). Studies of high–pressure mineral physics linked these seismic jumps to phase transitions in the mantle mineral olivine at 410 and 660 km depth [*Akaogi et al.*, 2007; *Bina*, 2003; *Bina and Helffrich*, 1994; *Fei et al.*, 2004; *Ita and Stixrude*, 1992; *Katsura and Ito*, 1989; *Katsura et al.*, 2004; *Ringwood and Irifune*, 1988]. Seismic methods for global mapping of these discontinuities came to the forefront with the development of the *SS* precursor method [*Flanagan and Shearer*, 1998; *Gu et al.*,

1

2003; *Shearer*, 1990; *Shearer and Masters*, 1992]. Due to the pressure–temperature behaviour of the olivine phase transitions at 410 and 660 km, both discontinuities are expected to display measurable depth variation under varying temperature regimes. The seismic reflection from the *410* is observed globally in stacked seismograms as a precursor to *SS*. This discontinuity, caused by the phase transition of the mantle mineral olivine into its higher pressure polymorph wadsleyite, is an exothermic reaction with a positive Clapeyron slope of $\sim$3.0 MPa/°K [*Helffrich*, 2000]. Due to this, the discontinuity is expected to deflect upwards when in contact with a negative thermal anomaly and to depress when encountering abnormally hot mantle material. The *660*, primarily the result of the decomposition of the olivine polymorph ringwoodite into magnesiowustite and perovskite [*Akaogi et al.*, 2007; *Bina*, 2003; *Helffrich*, 2000; *Ita and Stixrude*, 1992; *Katsura and Ito*, 1989], is expected to display the opposite behaviour. That is, the MTZ becomes thinner in the presence of hot thermal anomalies and thicker in colder (e.g., subduction) regions.

Observations of the depth variability of the MTZ discontinuities provide a valuable means for investigating the consequences of mantle composition and convection. As oceanic lithosphere is subducted along convergent margins, it descends into the mantle, where the geometry and fate of the downwelling, often water rich, lithosphere could vary substantially among subduction zones worldwide (e.g., *Fukao et al.* [2009]). Subduction style can be broadly classified by the degree of horizontal deflection that occurs as the slab impacts the dense and highly viscous lower mantle beneath the *660* [*Fukao et al.*, 2009; *Torii and Yoshioka*, 2007]. Slabs that undergo near–horizontal deflection have been termed "stagnant", as they have a tendency to remain at depths between 400–1000 km in the mantle rather than continuing downwards. By determining the depths of MTZ discontinuities, we are able to determine the slab geometry near the base of the upper mantle, providing constraint

on the style of subduction.

Two teleseismic methods commonly used to investigate MTZ structure are utilized in this thesis. In South America, a region with relatively sparse seismic station coverage, we apply the *SS* precursor method [*Flanagan and Shearer*, 1998; *Gu and Dziewoński*, 2002; *Schmerr and Garnero*, 2007; *Shearer*, 1993; *Shearer and Masters*, 1992] to construct a reflectivity cross–section through the subduction zone of the Nazca slab beneath the South American continent, presented in Chapter 3. The *SS* precursor method, described in more detail in Chapter 2, uses the low–amplitude underside shear wave reflections from the MTZ discontinuities recorded at epicentral distances of 100°–180°. These low amplitude phases, termed the *SS* precursors due to their arrival before the surface reflection *SS*, are widely used to investigate mantle structure. The differential time between the main *SS* arrival and the precursor arrivals is directly related to the depth of the reflecting interface at the mid–point of the ray–path, as the path of the *SS* phase is virtually identical to those of the precursor phases, with the exception of the portion of the ray–path immediately surrounding the mid–point. This geometry produces a large number of *SS* bounce–points in oceanic areas, regions under–sampled by most other methods of analysis. Previous studies involving these phases have been primarily global in scope [*Flanagan and Shearer*, 1998; *Gu et al.*, 2003; *Houser et al.*, 2008; *Shearer*, 1990, 1991, 1993; *Shearer and Masters*, 1992] with some regionally–focused investigations [*Contenti et al.*, 2012; *Gu et al.*, 2012; *Schmerr and Garnero*, 2007]. Due to a relatively recent increase in the volume of teleseismic data, mostly recorded at stations of the USArray project [*Levander*, 2003], the increased *SS* bounce–point density has enabled a high–resolution survey of the regional mantle reflectivity structure. Whereas receiver functions have been analysed based on regional arrays (e.g., *Liu et al.* [2003]), the narrow aperture and relatively short deployment durations have limited the utility

of the data for studies at transition zone depths.

In Chapter 4, I present a study of the MTZ beneath Alberta using data recorded by the Canadian Rockies and Alberta Network (CRANE), a recently deployed seismic array with coverage provided by 18 semi–permanent stations deployed across Alberta [*Gu et al.*, 2011]. For this study, we use the receiver function method [*Langston*, 1977, 1979; *Vinnik*, 1977], which recovers a representation of the layered Earth structure beneath the recording station using P–to–S converted waves generated at discontinuities in the subsurface. The deconvolution of the vertical from the radial component seismograms removes the effect of the earthquake source and the instrument response, yielding a time series showing the arrivals of P–to–S phases. Previous large–scale geophysical research within Canada has largely been conducted in concert with the Lithoprobe project [*Bostock et al.*, 2010], a trans–Canadian, multi–disciplinary research effort focusing on mapping crustal structure. Unfortunately, the active–source nature of the Lithoprobe seismic experiments, and the linear geometry of previously deployed passive teleseismic arrays means that the mantle and MTZ structure beneath the Alberta Basin has been relatively under–sampled. The addition of the CRANE dataset to the pre–existing CNSN receivers allows for an improved analysis of MTZ structure in this region at a higher resolution compared to previous global SS precursor [*Flanagan and Shearer*, 1998; *Gu et al.*, 2003; *Houser et al.*, 2008; *Shearer*, 1990, 1991, 1993; *Shearer and Masters*, 1992] and receiver function [*Chevrot et al.*, 1999; *Lawrence and Shearer*, 2006; *Tauzin et al.*, 2008] studies.

1.1 Thesis Scope

The aim of this thesis is to better understand the seismic and tectonic characteristics of the mantle beneath both the South American subduction system and the Alberta

Basin. In order to do this I will present two studies, with results obtained via *SS* precursor imaging in the case of South America, and receiver function analysis within the Alberta Basin. These two study areas are interesting due to the potential for increased understanding of transition zone behaviour near areas of active and past subduction. In South America, the interaction of the Nazca slab with the MTZ provides information regarding the style of convection within the mantle, as well as results indicating significant compositional heterogeneities within the mantle at MTZ depths. The data from the CRANE array in Alberta provides an opportunity to directly investigate the sharp velocity structure of the mantle in a region of the globe previously under–sampled by these methods. In this region, constraint on mantle structure has previously been largely provided by smooth mantle tomographic imagery (*Fukao et al.* [2009]; *Grand* [1994]; *Montelli et al.* [2004]; *Obayashi et al.* [2006] and references therein), which is preferentially sensitive to bulk variations in seismic velocity rather than to the depths of abrupt mantle discontinuities.

By investigating the mantle beneath South and North America, we aim to gain insight into the following questions:

- To what extent can we infer the presence or lack of subducted oceanic lithosphere within the MTZ from the depth variability of the *410* and *660*?

- Are we able to use depth variations of MTZ discontinuities in this region to reveal thermal and chemical heterogeneities in the mantle away from the subduction zone?

1.2 Thesis Overview

Chapter 2 introduces the methods used in the thesis. Both the *SS* precursor and receiver function methodologies are introduced and discussed. As well, the application of Singular Spectrum Analysis (SSA) for noise removal and spatial interpolation of receiver functions is presented, followed by the least–squares Parabolic Radon Transform (PRT) used to accurately determine the depth of MTZ discontinuities from the receiver function dataset.

Chapter 3 investigates the mantle reflectivity structure beneath the Nazca Plate subduction zone in South America using the *SS* precursor method. Using this approach we are able to construct a high–resolution mantle reflectivity image delineating the depth and amplitude variability of the MTZ across the transition from oceanic to cratonic mantle, which are separated by a zone of highly anomalous structure corresponding to the Nazca plate subduction zone. We obtain several main conclusions as a result of this analysis. First, the Nazca slab potentially stagnates at the base of the transition zone. Second, a reflection gap near 410 km depth is suggestive of compositional variations potentially related to retrograde trench migration. Lastly, we observe strong variability of the *660* at the base of the upper mantle, perhaps indicative of strong slab deformation in this region.

Chapter 4 presents the results of a receiver function study of the mantle beneath the CRANE array, which includes much of the Alberta basin with some coverage extending into the Rocky Mountains and Canadian Cordillera. The estimated receiver functions are subjected to SSA de–noising and interpolation, followed by the use of the PRT for reliable interface depth determination. Using this approach, we are able to determine that the MTZ beneath the array has a thickness near the expected global average with the exception of the south–easternmost three stations;

these three stations are thicker than expected by ~11 km, which we interpret as evidence of slab material at these depths. We also find that the MTZ conversions across the array are delayed relative to the expected arrival times, indicating the potential for upper mantle velocity structure in excess of that contained within published velocity models.

Chapter 5 summarizes the results obtained in the thesis and provides recommendations for future work.

CHAPTER 2

Theory and Methods

2.1 *SS* Precursors

An *SS* precursor trace consists of the transverse shear component of three–component earthquake recording, that reveals the seismic response of the Earth beneath the event–station midpoint. The *SS* phase is a transverse shear wave that reflects once at the surface, with the precursors to the *SS* phases consisting of underside reflections from discontinuities within the mantle (shown in Figure 2.1). Due to the shorter ray-path of the precursor phases (as they do not travel the full distance to the surface at the midpoint), they arrive prior to the arrival of the main *SS* phase. As the paths of the *SS* and precursor phases are similar away from the mid-point (the term bounce-point is also used interchangeably), we assume that the delay time between *SS* and its precursors (referred to as *SdS* phases, *d* denoting the depth of the reflecting interface) is primarily sensitive to structure near the midpoint. Figure 2.2 shows a synthetic *SS* trace computed via the reflectivity method [*Fuchs and Müller*, 1971] for an epicentral distance of 130°through PREM [*Dziewoński and Anderson*,

1981]. The precursor arrival time window has been vertically exaggerated by four times in order to clearly show the reflected precursor phases. To ensure near–vertical incidence of the incoming rays, we limit the distance range of the event–stations pairs to those containing arrivals between 100°and 180°. The sensitivity of this method to the structure near the midpoint of the ray–path, as opposed to structure near either the originating event or receiving station, allows investigation into areas with limited or non–existent station coverage, such as beneath oceans or in onshore regions where deployment of stations is difficult.

The first step in processing the precursor dataset is to align all the recorded seismograms using the main surface reflection phase. The data are then generally sorted into common midpoint (CMP) bins, in order to group seismograms sampling a similar geographical area. The bin size used varies considerably between individual studies, depending on such factors as the density of recorded data and the region under investigation. A small difference in ray parameter between the surface reflection and the phases reflecting from MTZ discontinuities means that the precursors have some move–out relative to the main phase. That is, the differential time between the main and precursory phases is a function of the distance between the event and station. In order to account for this, we apply a depth–conversion prior to the stacking. This time–to–depth conversion uses theoretical travel–times computed through a reference velocity model (PREM, [*Dziewoński and Anderson*, 1981]). After conversion, the precursor energy in each individual seismogram is aligned at the proper depth, and linear stacking is possible. Other techniques may be used to account for the precursor phase move–out, such as summation along ray parameter in the time–domain, known as slant stacking. Then, the data in each CMP bin are stacked to attenuate noise and amplify the coherent precursor phases. Lastly, once the data in each CMP bin are stacked, we estimate the approximate uncertainty in the amplitude and depths
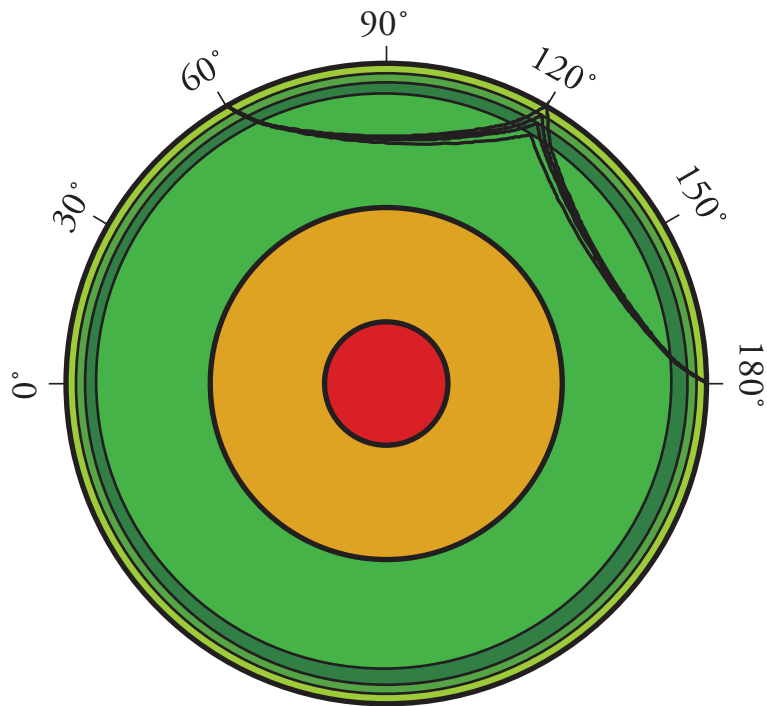
Figure 2.1: Schematic representation of the ray–paths of the *SS* and sub-surface reflected *SdS* arrivals. The global layering pattern is shown in color, with the shades of green representing the mantle, orange the outer core, and red the solid inner core.

of the results through a bootstrapping procedure. The time–to–depth conversion and stacking procedure is repeated for many random subsets of the data, and the standard deviation in amplitude of the resulting realizations provides a quantitative assessment of the reliability of the stacked data.

2.2 Receiver Functions

In contrast to the geometry of the SS precursors described in the previous section, the receiver function method is highly station–dependent. A receiver function is computed from the radial shear and compressional components of an earthquake recording, showing the seismic response of the Earth structure beneath the recording station. Figure 2.3 shows the ray–path of the incoming P wave as well as the ray–path of the converted Ps phase. The waveforms on the receiver function (RF) time–series show the arrivals of both the direct P–to–S conversions as well as multiple phases that reverberate beneath the seismic station (See Figure 2.2). The amplitudes of the arrivals depend on the incidence angle of the incoming P–wave–field and the magnitude of the velocity contrast between the layers producing the conversions. The delay times of the arrivals depend on the ray parameter of the incoming P–wave, the depth of the converting interface, and the velocity structure (both P and S) between the conversion depth and the surface. Several assumptions are commonly made during the course of receiver function analysis. We assume that the velocity structure beneath the station is laterally homogeneous and isotropic, that the layers responsible for the conversions are flat, and that the incident wave–field is planar. In most studies, these assumptions are approximately true, although in some regions the assumption of isotropy and lateral homogeneity is challenged, and the potential invalidity of these assumptions may appear as azimuthal variations in the amplitude

and delay times of the converted phases.

The computation of the individual receiver functions requires the separation of the incident and scattered wave–fields. In order to obtain near–vertical P–arrivals, we confine the distance range between event and station to 30°–90°. With a near–vertical P–wave ray–path, we assume that the vertical component seismogram represents the incident wave–field, and the converted (scattered) waves are contained in the radial component. Next, we normalize for the source–signature of each event. We may express the data using a convolutional model; the recordings are represented as the convolution of the Earth's near–station impulse response with the combined earthquake source–time function, far–field response, and instrument response of the seismometer. In this formulation, the near–station response is the receiver function we are attempting to isolate, and the combined source–time function, instrument response, and far–field effects are approximated by the vertical component recording. Then, the radial receiver function may be found by the deconvolution of the compressional (Z) component seismogram from the radial (R). Early solutions to this deconvolution problem were found through spectral division, with the addition of a "water–level" parameter to avoid division–by–zero errors and a Gaussian filter to provide stability in the presence of noise and the inaccuracy of the source–instrument wavelet. The water–level and Gaussian parameters were generally chosen qualitatively and could vary for each recording. Our approach is more well suited for automatic processing, by solving the deconvolution problem iteratively in the time–domain. We use the *iterdecon* program [*Ligorria and Ammon*, 1999], which iteratively approximates the receiver function. The iterative deconvolution operates by computing the cross–correlation of the Z and R components, and extracting the lag–time and amplitude of the highest correlation. For each iteration, a spike is added to the receiver function with an amplitude proportional to the magnitude
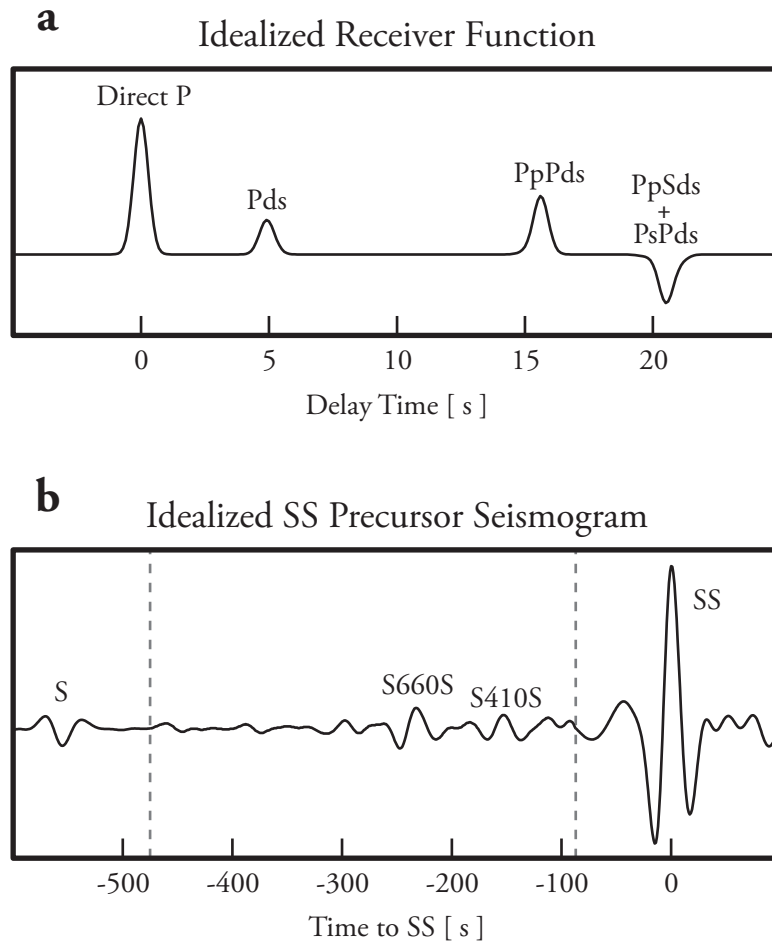
Figure 2.2: Idealized traces for both the methods discussed in this chapter. a) Receiver function trace computed at a distance of 60°for a simple Earth model. The phase arrival times are relative to the main P pulse. Shown are the P, Moho–converted Ps, and reverberated $PpPs$, $PpSs$, and $PsPs$ phases. b) SS precursor trace computed for a distance of 130°, with arrival times relative to the main SS phase. Shown are the SS, $S410S$, $S660S$, and S phase arrivals. The portion of the trace between the dashed lines has been vertically exaggerated by a factor of four to more clearly display the precursory arrivals.
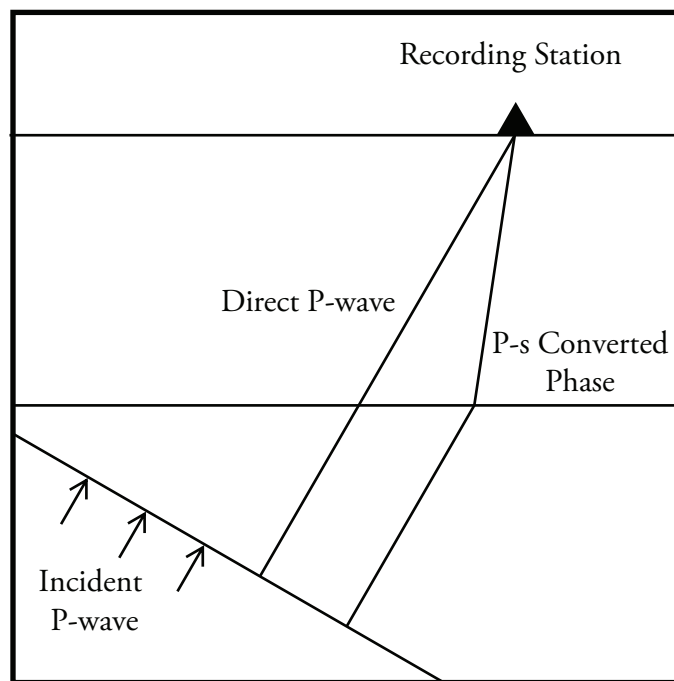
Figure 2.3: Schematic representation of the ray–paths of the P and subsurface converted Ps arrivals.

of the cross–correlation coefficient and a delay time determined by the time lag of that coefficient. At each new iteration, the contribution to the R component formed by the preceding iterations is removed from the data prior to the cross–correlation with Z. This allows for automated processing; rather than qualitatively choosing parameters trace–by–trace as in the spectral division, the seismologist simply chooses a maximum number of spikes to be added, as well as a stopping criterion based on the percentage match between the modelled data and the original radial seismogram.

2.3   Singular Spectrum Analysis

In order to increase the coherency of deep converted phase arrivals in receiver function data, which, due to the increased delay time and low amplitude of the phases, tend to have an increased noise level, we apply a de-noising procedure prior to the determinatin of the arrival times of the phases. The Multichannel Singular Spectrum Analysis (MSSA) is a noise attenuation method that operates on data in the frequency–space (f–x) domain [*Oropeza*, 2010; *Oropeza and Sacchi*, 2009; *Trickett*, 2003]. The premise is that linear events in the time–space (t–x) domain can be represented via superposition of complex sinusoids in the frequency–space domain. When this superposition of sinusoids is embedded in a Hankel matrix, one can prove that the theoretical rank of the Hankel matrix is K where K is the number of linear arrivals in the data. The latter is used to design noise attenuation methods that are based on rank–reduction techniques. In other words, if the data are contaminated with noise, the associated Hankel matrix will be of rank >K. Therefore, singular value decomposition (SVD) can be used to find an approximate representation of the lower rank Hankel matrix. This process was extended by *Oropeza* [2010] to the problem of seismic data reconstruction. In essence, missing observations (in this

case, empty receiver functions bins after the partial–stacking procedure) will have the same effect as that caused by random noise; that is, the rank of the Hankel matrix of the observations increases. Rank reduction of this matrix followed by back–transformation into the time–space domain may consequently be used to retrieve missing data. It is interesting to note that the concept of data reconstruction via rank–reduction methods is not only applicable to seismology. An important body of work exists in the so called "Matrix Completion" field. This is a field of mathematics that attempts to reconstruct matrices and/or tensors that have been corrupted by noise or erasures by using the assumption of low dimensionality [*Candes and Recht*, 2009]. Further details pertaining the implementation of the MSSA reconstruction can be found in *Oropeza* [2010].

2.4   Parabolic Radon Transform

In order to accurately determine the arrival time of the MTZ converted phases, we apply the Parabolic Radon Transform (PRT) to both the regional dataset and each individual station gather. The PRT is an integral transform where the amplitude of the Radon image at the location (τ, p) is determined by the integration through the spatial domain data along an integration path defined by individual (τ, p) pairs. This is described formally as

$$R(\tau_k, p_i) = (1/N_\Delta) \sum_{j=1}^{N_\Delta} M(t_k - T(p_i, \Delta_j, \delta), \Delta_j). \qquad (2.1)$$

where $M(t, \Delta)$ is the spatial domain data, $T(p_i, \Delta_j, \delta)$ is the function that describes the path of integration in the spatial domain, and R is the projection of M into the Radon domain. The parameter p_i determines the degree of curvature of the

integration path, and δ specifies the reference distance used for the transform (generally taken to be near the mean of the individual event–station distances Δ_j). The Radon time τ represents delay time at the reference event–station distance δ. Coherent signals along the integration path described in Equation (2.1) will sum constructively to a point in the Radon domain, with a potential maximum SNR increase of $\sqrt{N}$ where N is the number of input seismograms [*Shearer*, 1991].

Radon–type methods commonly in use in the seismological community, such as slant–stacking and H–k crustal analysis, use a linear path function T to approximate the move–out of the converted phases. However, at MTZ depths these arrivals are highly non–linear, and as such we utilize a higher–order path function, and approximate the move–out curves with parabolae.

In order to exploit the robustness provided by the least–squares approach, we pose the PRT as a regularized inverse problem. To do this, we require the operator that models the spatial domain data M given the Radon domain projection. This will define the forward problem whose adjoint is given by Equation (2.1). The forward problem is described as

$$M(t_k, \Delta_j) = \sum_{i=1}^{N_p} R(\tau + T(p_i, \Delta_j, \delta), p_i). \tag{2.2}$$

where the quantities in Equation (2.2) correspond with those in Equation (2.1). We then take advantage of the shift theorem in the Fourier domain to re–formulate Equation (2.2) as

$$M(\omega_k, \Delta_j) = \sum_{i=1}^{N_p} e^{-i\omega_k T(p_i, \Delta_j, \delta))} R(\omega_k, p_i) \tag{2.3}$$

which, for a constant frequency, may be expressed in matrix notation as

$$M = AR \tag{2.4}$$

where A is the operator that computes the forward problem, modelling the data M given the Radon panel R [*An et al.*, 2007; *Gu and Sacchi*, 2009; *Sacchi and Ulrych*, 1995]. Correspondingly, Equation (2.1) becomes

$$R = A^T M \tag{2.5}$$

where A^T is the adjoint of A.

However, this is an ill–posed problem, without a guarantee of stability or uniqueness in the solution [*Olafsson*, 2006; *Tikhonov*, 1987]. We introduce Tikhonov regularization based on the ℓ^2 norm of the model in order to stabilize the inversion, resulting in the following least–squares cost function to be minimized:

$$J = \|M - AR\|_2 + \mu\|R\|_2 \tag{2.6}$$

where μ denotes the regularization parameter, which controls the relative contribution of the model norm versus that of the data misfit norm. The appropriate μ value is determined empirically, by constructing a trade–off curve of the data misfit $\|M - AR\|_2$ vs. the model norm $\|R\|_2$, for varying levels of regularization. For each inversion, the value nearest to the corner of the trade–off curve is chosen as the final μ. The PRT in this study is computed using the forward and adjoint subroutines provided by *Schultz and Gu* [2012]. These subroutines solve the problem defined in Equation (2.6) by explicitly constructing the matrix A, and solving the damped

normal equations:

$$R = (A^T A + \mu I)^{-1} A^T M \tag{2.7}$$

to determine the model R.

CHAPTER 3

Shear Wave Reflectivity Imaging of the Nazca-South America Subduction Zone: Stagnant Slab in the Mantle Transition Zone? [1]

3.1 Introduction

The Nazca plate has been subducting under the western margin of the South American continent since at least the late Cretaceous period [*Bird*, 2003; *Pardo-Casas and Molnar*, 1987; *Russo and Silver*, 1996]. This long–lasting ocean–continent convergence, which is ongoing at a present–day rate of 3–8 cm/yr [*Bevis et al.*, 1999, 2001; *Klotz et al.*, 1999; *Kreemer et al.*, 2003; *Norabuena et al.*, 1998], is directly

responsible for the formation of the Andean mountain chain and the associated seismic activity along the Wadati–Benioff zone [*Barazangi and Isacks*, 1976; *Cahill and Isacks*, 1992; *James and Snoke*, 1990]. The substantial surface topography of the region is mirrored by complexities in subduction zone morphology and dynamics, as evidenced by observations from recent seismic tomographic analyses [*Bijwaard et al.*, 1998; *Engdahl et al.*, 1995; *Fukao et al.*, 2009; *Grand*, 1994; *Li et al.*, 2008; *Ritsema et al.*, 2004; *van der Lee et al.*, 2001]. Continuous high velocity anomalies have been suggested to extend into the lower mantle in both northern and central South America [*Engdahl et al.*, 1995; *Li et al.*, 2008], whereas stagnation and/or ponding of subducted oceanic lithosphere is possible within the Mantle Transition Zone (MTZ) or at shallow lower mantle depths towards the south [*Engdahl et al.*, 1995; *Fukao et al.*, 2001, 2009; *Li et al.*, 2008]. Studies based on secondary reflected/converted body waves offer additional constraints on the gradients of mantle seismic velocities. A regionally depressed 660 km discontinuity (hereafter, all discontinuities will be referred to by the theoretical depth at which they occur, e.g., *660*) has been reported by studies of *SS* precursors [*Flanagan and Shearer*, 1998; *Gu and Dziewoński*, 2002; *Schmerr and Garnero*, 2007; *Shearer*, 1993; *Shearer and Masters*, 1992] and *P–to–S* converted waves [*Liu et al.*, 2003; *Tauzin et al.*, 2008; *Wölbern et al.*, 2009], which suggests a substantial low temperature anomaly near the base of the upper mantle.

The data constraints on the *410* and *660* phase boundaries under the South America convergent zone have traditionally been problematic due to low data density [*Flanagan and Shearer*, 1998; *Gu et al.*, 1998, 2003] as well as the uneven sampling and limited depth extent of receiver function analysis [*Heit et al.*, 2007; *Liu et al.*, 2003; *Wölbern et al.*, 2009], although recent efforts [*Schmerr and Garnero*, 2007; *Soudoudi et al.*, 2011] have shown significant improvements and future promise. These earlier studies have revealed a broad depression of *410* in the back–arc of

the subduction zone, as well as localized topography on both *410* and *660* due to the effect of the subducting Nazca plate. Still, further details of the olivine phase boundaries and the existence/nature of potential reflectors in the depth range of 300–1000 km warrant further verification and discussion.

In this study, we aim to provide a high–resolution analysis of mantle reflectors beneath the eastern Pacific Ocean, the Andean mountain chain, and the South American craton down to mid–mantle depths. Our time–to–depth migration of an up–to–date SS precursor dataset enables a detailed regional comparison between reflection amplitudes and seismic velocity, which is vital for a self–consistent model of subduction dynamics surrounding the MTZ.

3.2 Data and Methodology

The use of SS precursors, small amplitude underside reflections from known and theorized mantle interfaces, has long been documented [*Deuss and Woodhouse*, 2002; *Gu et al.*, 1998; *Gu and Dziewoński*, 2002; *Houser et al.*, 2008; *Lawrence and Shearer*, 2008; *Shearer*, 1991, 1993; *Shearer and Masters*, 1992] as a useful tool for quantifying the structure of the upper ∼1500 km of the mantle. We utilize over 30 years (1972–2009) of broadband and long–period earthquake waveform data archived by the Incorporated Research Institutions for Seismology (IRIS), the Canadian National Seismograph Network (CNSN) and the GEOFON program. Our data search and processing criteria are similar to those employed in *An et al.* [2007], although the maximum earthquake depth and epicentral distance are increased to 150 km and 160 degrees respectively. Figure 3.1 shows the global distribution of events and stations used to generate the SS precursor dataset. We utilize over 130 unique M_w >5.5 earthquakes recorded at over 900 global broadband, long–period, and high–frequency

seismic stations to construct our dataset of 5720 seismograms. Event locations are marked by red stars, with the blue triangles marking station locations. All event–station pairs fall within 100°–160°of epicentral distance. A large proportion of the dataset is provided by earthquakes located in the South Atlantic recorded at USArray stations in the western United States. The square box delineates the bounds of the study area; only event–station pairs with great–circle midpoints within this region are used.

To pre–process the dataset, we first apply a Butterworth band–pass filter with corner frequencies at periods corresponding to 20 and 65 seconds. We then introduce a Signal–to–Noise Ratio (SNR) criterion, defined as the ratio between the main amplitude of the SS phase and the root mean square peak amplitude of the 100 seconds preceding the SS arrival, and eliminate source–receiver pairs with SNR $\leq$3. We apply the Hilbert transform to correct the filtered waveforms for internal caustics in the wave field [*Rychert and Shearer*, 2010; *Shearer et al.*, 1999]. Finally, the traces are individually inspected, the polarity corrected to ensure that the primary amplitude of the SS phase is positive, and aligned to the SS phase with the help of reflectivity synthetic seismograms [*Fuchs and Müller*, 1971; *Herrmann and Wang*, 1985; *Kennett*, 1983] and theoretical SdS travel–times [*Crotwell et al.*, 1999; *Dziewoński and Anderson*, 1981]. Our final dataset contains a total of 5721 high quality seismograms densely sampling the Peruvian, Bolivian, and northern Chilean Andes, extending into the Amazonian basin of Brazil (Figure 3.2).

After aligning the seismograms to the first major swing of the SS phase, we apply corrections for topography, crustal structure, and mantle heterogeneity. Shown in Figure 3.3 are the corrections applied to the individual traces. The crustal (Figure 3.3c) and topographic (Figure 3.3b) corrections are computed using the CRUST2.0 [*Bassin and Laske*, 2000] and ETOPO2 [Data Announcement 88-MGG-
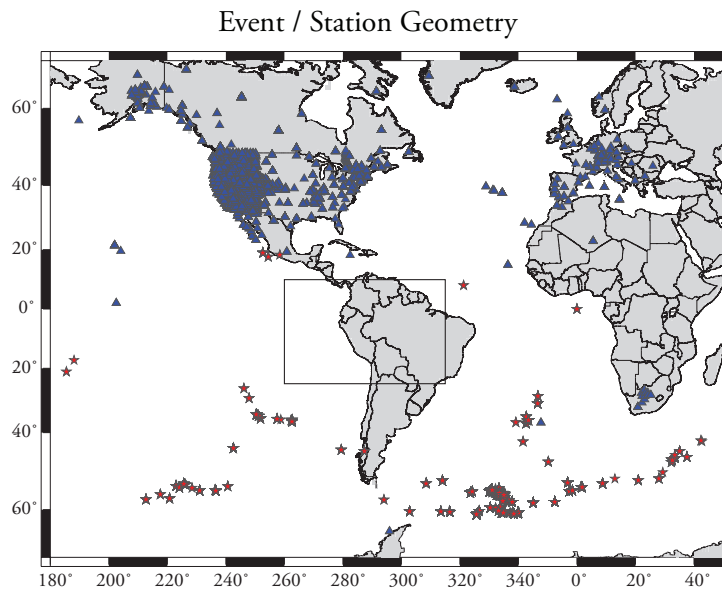
Figure 3.1: Global map showing the event locations (red stars), seismic station locations (blue triangles), and the study region (black rectangle).
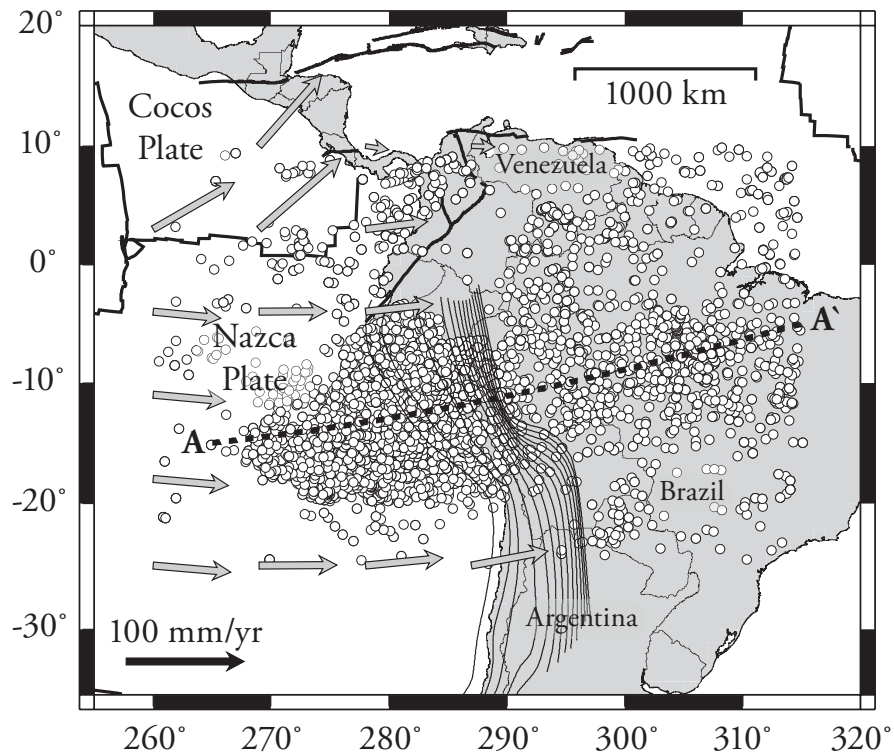
Figure 3.2: Midpoints of the 5720 seismograms used in this study, along with GPS plate motion vectors from the GSRM–1 model (filled arrows) [*Kreemer et al.*, 2003]. Slab contours are obtained from the Regionalized Upper Mantle (RUM) model of *Gudmundsson and Sambridge* [1998] (thin grey lines). The plate boundaries are plotted after *Bird* [2003] (thin black lines) and the surface trace of the cross section are represented using a thick black line.

02] models respectively. The correction for mantle heterogeneities (Figure 3.3b) uses the S12WM13 shear velocity model [*Su et al.*, 1995]. The three individual corrections are summed to obtain the total (Figure 3.3d) and applied as a time shift to the unmigrated data. The largest positive corrections occur along the Andean mountain chain, largely due to the effect of the severe topography and deep crustal root in that region, with 95% of the final corrections falling between -4.8 s and 2.7 s. The bulk of the negative values lie within the Pacific Ocean, attributed to the thin oceanic crust.

To estimate the mantle reflectivity structure (Figure 3.7) the data are sorted into Common Midpoint (CMP) gathers [*Shearer*, 1991; *Yilmaz*, 2001] along the great circle arc between cross–section endpoints. Due to the previously revealed geometry of the subducting Nazca slab [*Gudmundsson and Sambridge*, 1998] we tailor our stacking bins to maximize resolution through our cross section by utilizing thin rectangular bins with a dimension of 4°x 8°, with the long axis of the bin aligned at 90°to the strike of the cross-section. This geometry is used to maximize the nominal resolution along the dip of the Nazca slab while maintaining a sufficient number of data in each bin for effective noise suppression. The time series are then mapped to depth using theoretical *SdS* travel–times [*Crotwell et al.*, 1999; *Gu et al.*, 1998, 2012; *Rondenay*, 2009; *Rost and Thomas*, 2009]. The accuracy and resolution of the method is evaluated from a synthetic dataset computed for all source–station pairs. The PREM synthetic seismograms generated to aid in the manual phase alignment are subjected to the same pre–processing steps as the original dataset, with the exception of the SNR criterion and the static corrections. The resulting migrated stack (Figure 3.4) shows consistent arrival times and amplitudes on both *410* and *660* along the cross section, with the exception of the eastern corner of the study area (see Figure 3.2) where the data fold is low. This artefact in the synthetic stack is attributed to the limitations of the reflectivity method when computing
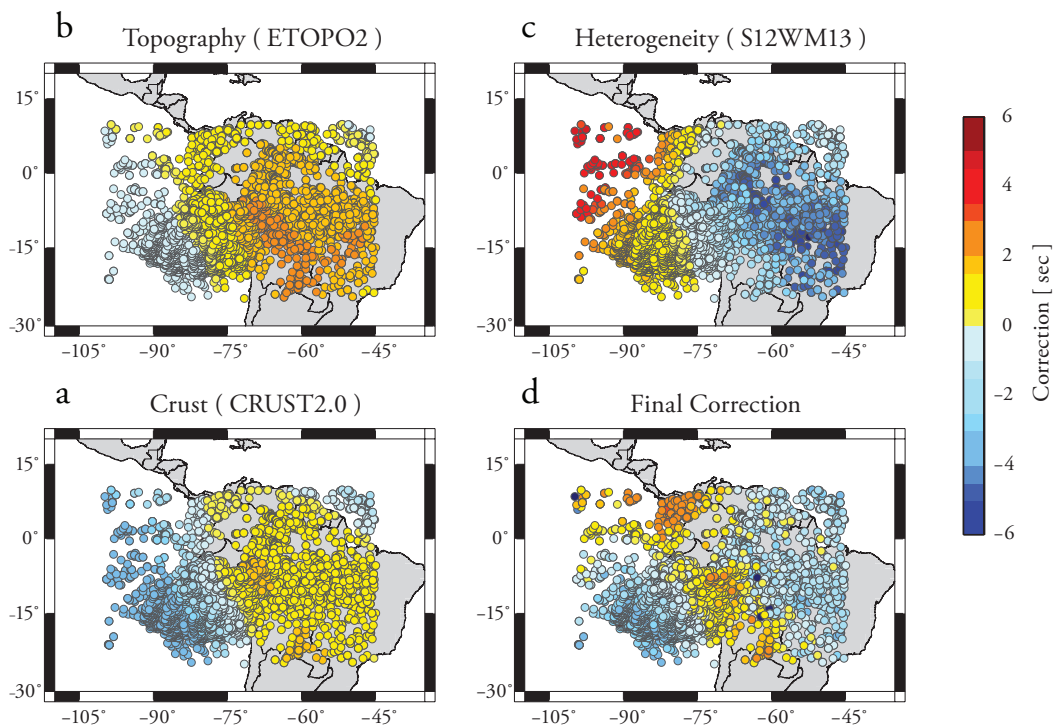
Figure 3.3: Regional map showing the corrections applied to the data traces. a) Crustal correction calculated using the CRUST2.0 model b) Topography correction calculated using the ETOPO5 model c) Heterogeneity correction calculated using the S12WM13 shear velocity model d) Total correction applied is the sum of a)–c)

seismograms at large epicentral distances.

Lastly, in order to eliminate structures with large uncertainties, we produce a composite cross section by subtracting one standard deviation of the bootstrap uncertainty from the migrated reflectivity data. Figure 3.5 shows an estimate of the uncertainty in our mantle reflectivity estimate constructed using a modified bootstrap re–sampling approach [*Efron and Tibshirani*, 1991; *Shearer*, 1993]. Our method is as follows: (i) 100 "bootstrap samples" are constructed by randomly drawing, with replacement, 50% of the data traces along the cross section. (ii) Rather than computing the mean of these data as in *Efron and Tibshirani* [1991], we apply migration to produce a reflectivity cross–section. (iii) The standard deviation of the reflection amplitude at each pixel of the image is computed to provide a quantitative measure of the uncertainty at that location. The final error map then indicates which regions of our final migrated reflectivity cross–section are more affected by inconsistent reflection amplitudes. The uncertainty results show increased amplitude variability in the eastern portion of the cross section; however the highest uncertainties are always in the upper 150 km of the mantle. This result may partially reflect a higher noise threshold due to lower data coverage in this region, compared to the high density of SS bounce points to the west. Alternatively, this result may arise from increased variability in the true reflection amplitudes from this region, due to the higher spatial variability and increasingly complex reflectivity structure beneath the Nazca subduction zone and South American continent. The introduction of this procedure preferentially suppresses the reflectivity amplitudes in regions with less robust data constraint.
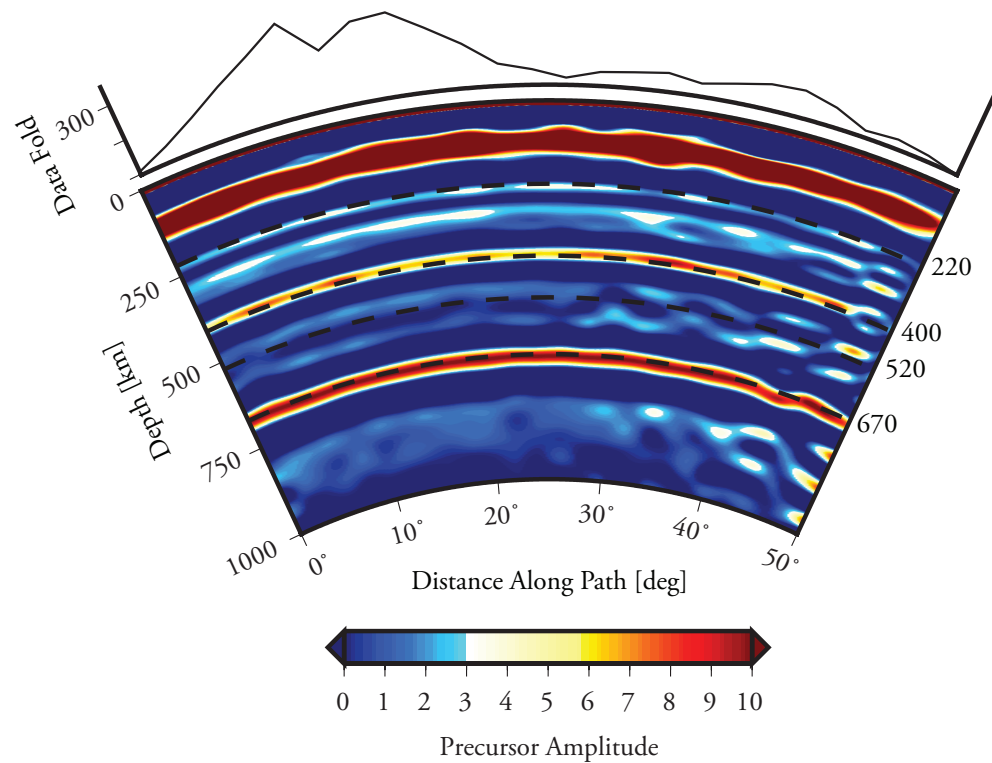
Figure 3.4: Upper panel shows the data fold (number of data traces per bin) along the cross–section path. Lower panel shows the migration procedure applied to synthetic seismograms. Synthetics are computed based on PREM [*Dziewoński and Anderson*, 1981]. The dotted lines indicate the depths of potential mantle discontinuities at 220, 400, 520, and 670 km.
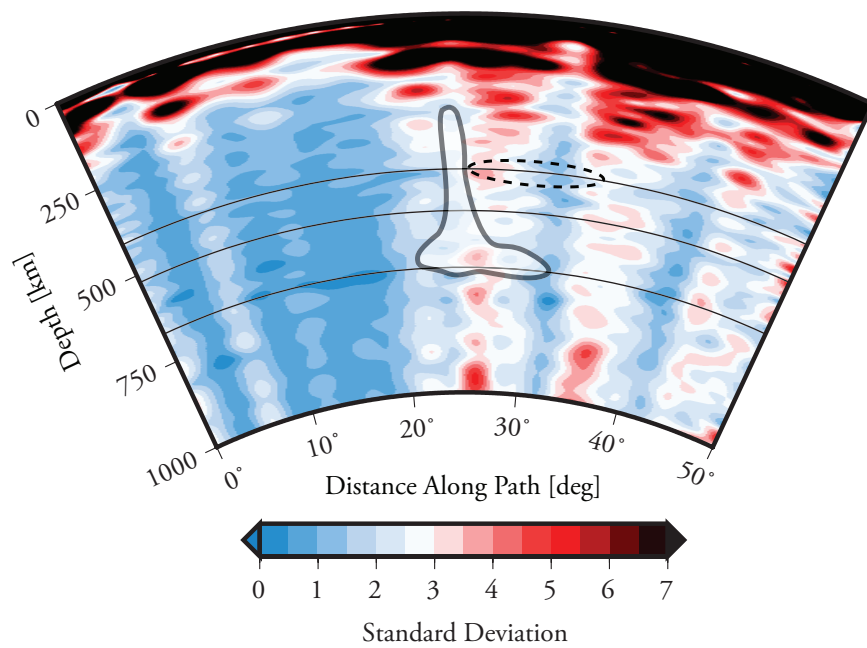
Figure 3.5: Cross–section showing the standard deviation of the bootstrap uncertainty computed for the data. The solid black lines indicate the depths of potential mantle discontinuities at 410, 520, and 660 km. The dashed black oval indicates the zone corresponding to the reflection gap in Figure 3.7a, and the solid grey line shows our interpretation of the location of the subducting Nazca slab.

3.3 Results

3.3.1 Regional Averages

Figure 3.6 shows depth migrated data from the three main tectonic domains in the study region (the Pacific Ocean, the Nazca subduction zone and continental South America) and the regional average based on all available *SS* precursor data. The large–scale averaging allows the determination of first–order, continent–scale structure present in the data set; the influence of overlapping data traces is eliminated through the wide spacing between stacking bins. Strong reflection amplitudes are observed at 421 km and 676 km in the regionally averaged stack resulting in an average MTZ thickness of 255 km (near the value of ∼257 km in *Gu and Dziewoński* [2002]). This value is on the higher end of the global average range of 240–260 km (e.g., *Flanagan and Shearer* [1998]; *Gu et al.* [1998]; *Gu and Dziewoński* [2002]; *Gu et al.* [2003]; *Houser et al.* [2008]; *Lawrence and Shearer* [2008]; *Tauzin et al.* [2010], though a broadened MTZ beneath South America is largely consistent with these earlier global analyses. Clear arrivals from mantle reflectors are also present at regional depths of 525 km (comparable to the depth reported by *Shearer* [1990] in the same region), 315 km and 900 km with the respective amplitudes of 60%, 80% and 50% of the *660*.

Of the three regions, the migrated *SS* precursors beneath the Amazonian craton are most consistent with the regional averages (Figure 3.6). The depths of the MTZ discontinuities (*410*, *520*, *660*) are 420, 525 and 671 km, respectively, all within 5 km of the regional averages. The *410* reflection in this bin is nearly twice the amplitude of the regional average stack. The lower mantle shows multiple maxima (at ∼800 km and ∼875 km), both exhibiting reflection amplitudes similar to the *660*.
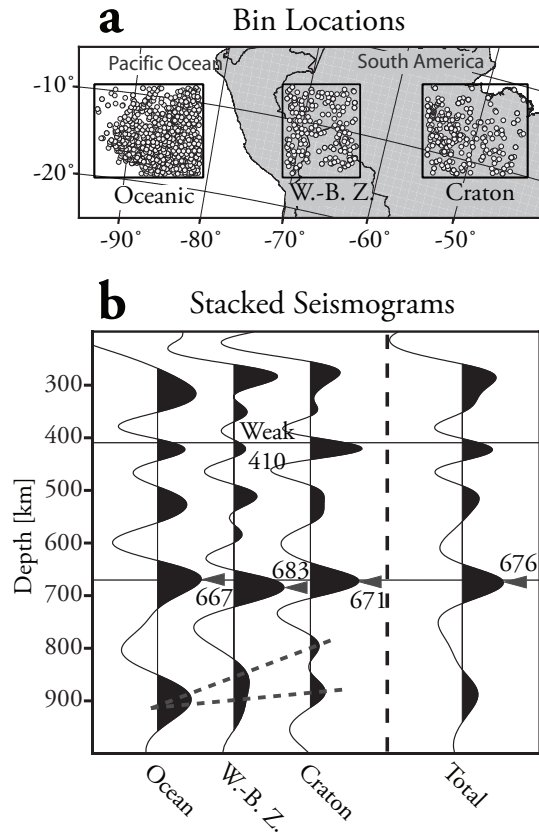
Figure 3.6: Stacks of *SS* precursors showing the large–scale reflectivity structures across the region. Bin locations (a) are shown encompassing the three regimes present: oceanic, Wadati–Benioff Zone (W.–B. Z) and cratonic. The bins are 10°in width with variable length. The traces (b) show consistent arrivals corresponding to the MTZ discontinuities (*410*, *520*, and *660*) as well as upper mantle (300 km) and lower mantle (850–900 km). The local depths of the *660* are as labelled and show a clear depression near the Benioff zone (the centre bin). The amplitude of the *410* is diminished in regions of subduction relative to the regional average.

In the Pacific Ocean (the westernmost bin) the *660* shows similar reflection amplitudes and an earlier arrival time (corresponding to ∼9 km of elevation) relative to the regional stack. An anomalously strong *520* reflection is observed within the MTZ, with the reflection amplitude nearly doubling the regional estimate. This feature is consistent with recent findings from receiver functions [*Liu et al.*, 2003] and supports the preferential detection of the *520* under oceans [*Deuss and Woodhouse*, 2002; *Gu et al.*, 1998]. A reflection peak centred near 900 km depth is observed in the lower mantle portion of the seismogram.

Near the Benioff zone, the central bin shows a considerably weakened *410* at ∼417 km, 4 km shallower than the regional average but still depressed relative to the global average of 410 km [*Deuss and Woodhouse*, 2002; *Gu et al.*, 2003; *Houser et al.*, 2008] (Figure 3.6). The magnitude of the amplitude drop–off (>50%) has not been previously documented in other major subduction zones and cannot be fully attributed to thermal variations associated the descending Nazca plate. A strongly depressed *660* further accentuates the anomalous mantle reflectivity structure beneath the convergent zone, though unlike the *410*, the amplitude of the *660* shows no visible influence from subduction–related processes. Below the MTZ, we detect a lower mantle reflector at ∼850 km depth, shallow relative to the oceanic and cratonic stacks. The broad waveform associated with this lower–mantle structure highlights an eastward transition from a high–amplitude, single reflector under the Nazca plate to two relatively weak signals under the Amazonian craton. The severely diminished *410*, the deep *660*, and the characteristics and potential origin of lower mantle reflector(s) in this region are further examined through a higher–resolution reflectivity cross–section presented below.

3.3.2 High Resolution Reflectivity Structures

Figure 3.7 shows the high–resolution reflectivity structure constructed from *SS* precursors reflecting beneath the Pacific Ocean and the South American continent. To eliminate structures with large uncertainties, we produce a composite cross section by subtracting one standard deviation of the bootstrap uncertainty from the migrated reflectivity data. The uncertainty is computed using a modified bootstrap approach [*Efron and Tibshirani*, 1991] using 100 re–sampled data subsets randomly selected, with replacement, from the pre–migration *SS* precursor dataset. The introduction of this procedure preferentially suppresses the reflectivity amplitudes in regions with less robust data constraints.

The mantle beneath the western segment (5°–20°along path) is dominated by five sub–horizontal reflectors at approximate depths of 300, 420, 520, 660, and 900 km. The MTZ reflectors (*410*, *520*, *660*) in this region show minimal depth variation, with all three reflectors occurring at depths similar to the wider–area ocean average presented by Figure 3.6. A slight depression and weakening in amplitude of the *410* is observed near the centre of this distance range; however, this anomaly may be an artefact of the corrections applied to account for crustal thickness variations.

Broad, laterally coherent reflections observed east of the Nazca–South America subduction zone are similar in character to the upper mantle reflectivity structure beneath the Pacific Ocean. The 410 km discontinuity is depressed, occurring at 430 km, while the *660* is relatively unperturbed immediately to the east beneath the craton. Intermittent reflections from the *520* are visible at 45°and 47°along path at depths of 540 and 500 km. Minimal topography is observed along the boundaries of the MTZ beneath the Brazilian Shield (35°–40°along path), with the exception of a weak and slightly raised (by <10 km) *410* beneath the Brazilian Shield near
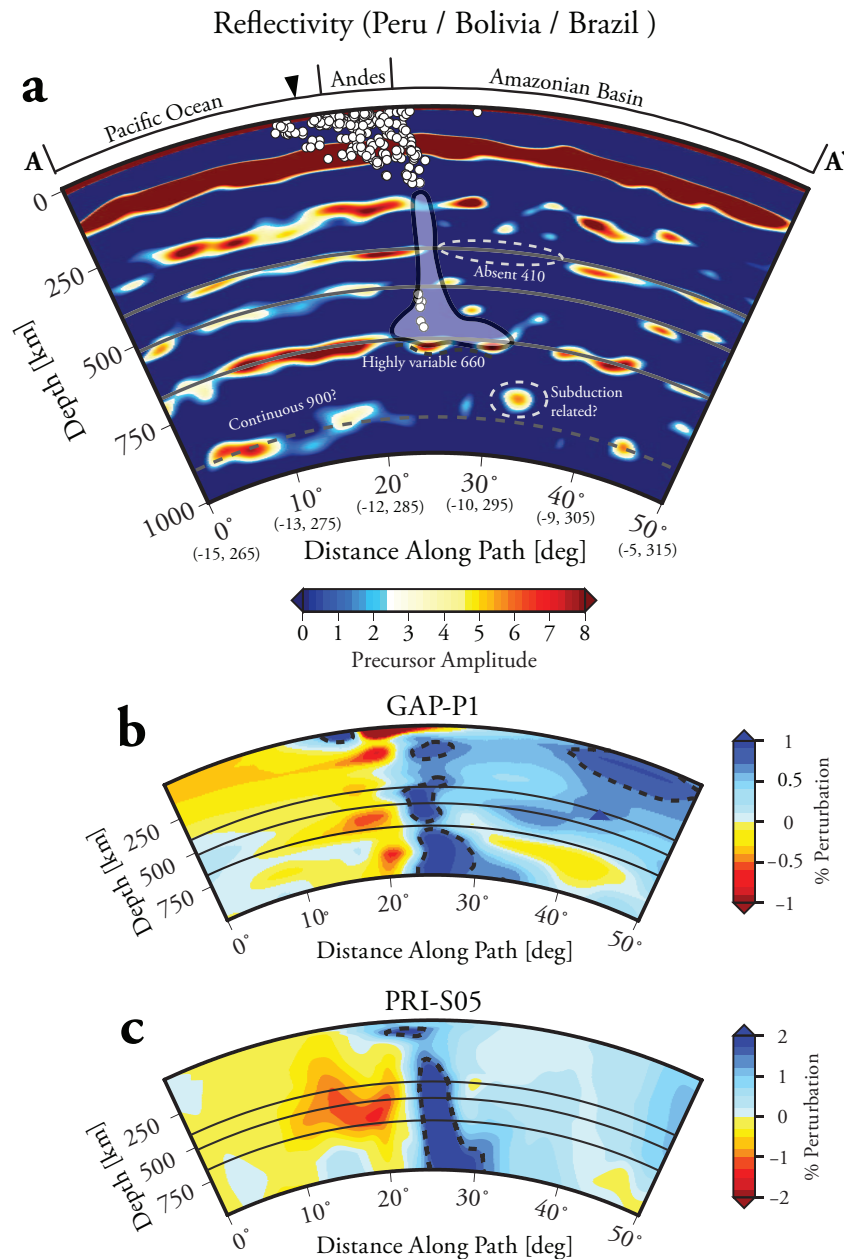
Figure 3.7: (a) Reflectivity cross–section across South America (see surface trace in Figure 3.2). The white outline shows the interpreted position of the subducting Nazca slab. The *410*, *520*, and *660* discontinuities are marked by black lines. Also shown are velocity perturbation through both (b) the GAP–P1 velocity model and (c) the PRI–P05 velocity model. The dashed black lines on the velocity models are the +1.5% and +0.7% velocity contours for PRI–S05 [*Montelli et al.*, 2004] and GAP–P1 [*Obayashi et al.*, 2006], respectively. The circles indicate earthquake hypocentres along the cross–section.

42°distance along path.

The mantle under the Andean convergent zone (22°–35°) is considerably more complex than within the adjacent tectonic domains (see Figure 3.7a). The reflections beneath the Andes show robust amplitudes near *410* and ∼280 km depth. The depth of *410* undergoes ∼10 km of uplift relative to the regional average, which is not observed in regional average stacks (Figure 3.6) due to its limited lateral scale. A wide (∼15°) reflection gap is detected in the back–arc of the subduction zone, where the amplitude of *410* is reduced to <3% relative to *SS*. Two distinct MTZ reflectors are observed along trench dip at 500 km and 600 km, while the base of the MTZ shows two depressed zones (by ∼25 km) separated by areas of near–average depth and low amplitude (Figure 3.7a). A strong reflector with >5% amplitude is visible beneath central Amazonian basin where the overlying *660* falls below our detection threshold (Figure 3.7a). The diffuse nature of this reflector and its considerable vertical extension (>100 km based on a 3% amplitude cut-off, also see Figure 3.6) argues against a sharp mantle reflection.

3.4 Discussions

The general agreement between both our reflectivity cross–section and the results from large–scale stacking shows that key structures in this region persist at both high and low lateral resolutions. The higher–resolution reflectivity structure beneath the Pacific Ocean and South American continent, which consists mainly of relatively undisturbed sub–horizontal signals, is consistent with the broad averages obtained by regional averaging based on tectonic domains.

The previously mentioned depression of the *410* below the Brazilian Shield, also evident in an earlier study of the *410* below South America, [*Schmerr and Garnero,*

2007], may suggest the presence of a hot thermal anomaly affecting the MTZ discontinuities, yet not extending to the base of the MTZ as no corresponding uplift is observed on the *660*. Although the global tomographic models used (Figure 3.7b,c) do not contain a pronounced low–velocity anomaly in central/eastern South America, regional tomographic results consistently report slow wave propagation (up to -2.4% shear wave velocity) within the upper 200–400 km of the South American mantle that is perhaps associated with a late Jurassic plume beneath the Parana flood basalt province [*VanDecar et al.*, 1995]. An alternate explanation for the necessary temperature increase is the insulating effect of the thick cratonic root [*Phillips and Coltice*, 2010], which may impede heat flow in the region, resulting in a broad depression of the *410* below the continent.

The mantle beneath the Andes shows increased reflection amplitudes for both the *410* and a potential upper mantle reflector at an approximate depth of 280 km. In a recent study of the northern Honshu subduction zone [*Obayashi et al.*, 2006], a low–velocity upper mantle anomaly was identified seaward of the subducting slab. This thermo–chemical heterogeneity was subsequently interpreted as a stable region of silicate partial melt resting on the *410*. Such a lens may be formed by the release of water as a hot thermal structure rising from mid–mantle depths undergoes the wadsleyite $\rightarrow$ olivine phase change. Tomographic results in South America from the same model (Figure 3.7b, model GAP–P1), reveal a strong MTZ low–velocity zone as well as a series of secondary low–velocity heterogeneities immediately west of the Nazca slab (Figure 3.7b). The presence of a melt–rich zone would depress the *410* and decrease the impedance contrast across this phase boundary, neither of which is observed directly west of the Benioff zone. However, the potential for a small–scale depression of the *410* as a result of a localized warm upwelling should not be ruled out.

The observed slight uplift of the *410* in the Wadati–Benioff zone of the descending slab is expected, as an elevated *410* will occur in relatively cold regions due to the positive Clapeyron slope of the olivine to wadsleyite ($\alpha \rightarrow \beta$) phase transformation [*Bina and Helffrich*, 1994; *Katsura and Ito*, 1989]. The presence of subducted oceanic lithosphere in the MTZ is further corroborated by the 7 km depression of the *660* relative to the regional average. Assuming a pyrolitic mantle composition with 10% iron [*Ringwood*, 1975], this topographic low corresponds to a temperature decrease of 120℃[*Bina and Helffrich*, 1994] surrounding the ringwoodite to perovskite + magnesiowustite ($\gamma \rightarrow pv + mw$) transformation [*Bina and Helffrich*, 1994; *Irifune et al.*, 1998; *Ringwood*, 1975]. Overall, a shallow *410* and *520* (which occurs at 515 km) alongside a deep *660* suggests strong mantle heterogeneities down to, at the least, the base of the upper mantle beneath the convergent zone.

The reflectivity structure in the region stretching from beneath the Nazca trench to more than 1500 km into the back–arc exhibits strong local variations that are not present in the broad regional averages. The origin of the amplitude drop–off and depression of the *410* in the back–arc of the Nazca plate subduction (Figure 3.7a, Figure 3.8a) is enigmatic. While a high–temperature anomaly at the top of the MTZ could produce the observed depression, a distinctive low–velocity zone is not present in the tomographic models shown in Figure 3.7b,c. More importantly, a warm shallow mantle would increase the velocity contrast across the *410*, which is at odds with the observed amplitude reduction (Figure 3.7). Alternatively, incoherent stacking due to a dipping interface [*Chaljub and Tarantola*, 1997; *Gu et al.*, 2012; *Neele et al.*, 1997] could lower the *410* strength, but the topography of the *410* in this region is insufficient to cause major shear–wave scattering effects. Changes in mantle composition may be required to explain the observed *410* reflection gap. Trench rollback to the west [*Lallemand et al.*, 2008] and the formation of a hydrated

zone directly above the *410* [*Schmerr and Garnero*, 2007] can reduce the amplitude by broadening the olivine–wadsleyite phase loop. Such a hydrous lens [*Zheng et al.*, 2007] can also cause double reflections [*Schmerr and Garnero*, 2007] associated with the olivine–wadsleyite transition and the wet–dry wadsleyite boundary, although such waveform complexities appear to be more prominent in the *410* signals north of our study region. Recent numerical simulations by *Hier-Majumder and Courtier* [2011] have suggested a distributed layer of neutrally buoyant melt in the mantle between 350 and 420 km depth. Based on these models, a melt fraction of ∼1% is sufficient to explain the diminished reflection amplitude. Potential contributions of other mantle constituents could be evaluated based on our *410* observations in this region. For instance, the preferential extraction of iron in the mantle wedge could increase the weight percentage of magnesium in the descending slab [*Agee*, 1998; *Deon et al.*, 2011] and the pressure required for the olivine–wadsleyite transformation. This mechanism would both deepen and sharpen the interface; the latter effect is problematic given the diminished *410* amplitude, however.

Our observation of a deep *660* near the descending Nazca slab is consistent with earlier published results based on receiver functions and *ScS* reverberations [*Clarke et al.*, 1995; *Liu et al.*, 2003; *Wölbern et al.*, 2009]. Due to the negative Clapeyron slope of the ringwoodite to perovskite + magnesiowustite mineral phase transition [*Bina and Helffrich*, 1994; *Helffrich*, 2000; *Houser and William*, 2010; *Irifune et al.*, 1998; *Katsura et al.*, 2003], a delayed transition is expected in a cold subducting oceanic lithosphere. The magnitude of the $\gamma \rightarrow pv + mw$ Clapeyron slope (-1.3, *Fei et al.* [2004], -1.2, *Katsura et al.* [2003], -2.0, *Bina and Helffrich* [1994]) predicts a lesser deflection of *660* than of *410* (Clapeyron slope ranging from +2.5 *Katsura and Ito* [1989] to +4.0 *Katsura et al.* [2004]) under similar temperature regimes, although the opposite has been previously documented in global studies of
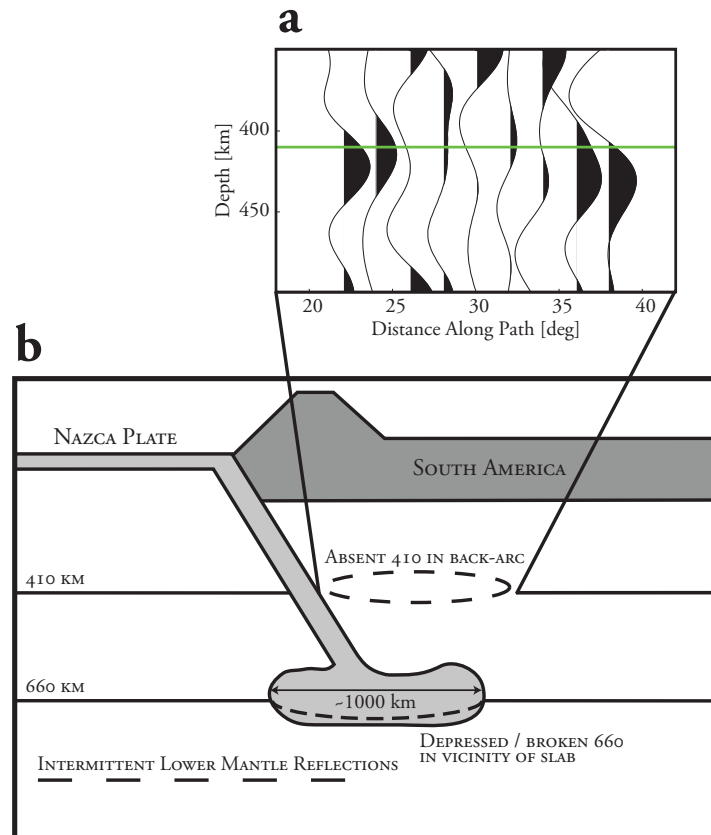
Figure 3.8: (a) Excerpt from the *SS* precursor dataset, highlighting the reflection gap on the *410*. The data include the two bins both preceding and following the gap. (b) A schematic representation of our main results and interpretations. Entrained hydrated material forms a lens on the *410*, creating a broad zone with little to no reflection. Partial slab penetration through the bottom of the MTZ causes depression in addition to missing or significantly reduced amplitudes on the *410*. Scattered reflections in the lower mantle potentially result from deep phase transitions, or could represent direct reflections from avalanched slab material.

MTZ discontinuity topography [*Flanagan and Shearer*, 1998; *Gu et al.*, 1998, 2003].

The reflectivity structure at the base of the upper mantle is complex in a 1200–1500 km wide zone east of the Peru–Chile Trench. This anomalous region contains distinct zones of depression under the Andes and Amazon Basin, as well as a reflection gap beneath central Brazil (Figure 3.7). We interpret the unique shape of the *660* as evidence of slab stagnation and buckling, deformation mechanisms that are likely facilitated by the high relative convergence rate of the Nazca–South America system [*Norabuena et al.*, 1998] and the observed ocean–ward migration of the Peru–Chile Trench [*Lallemand et al.*, 2008]. This interpretation (Figure 3.7, Figure 3.8b) is supported by recent results from reflector / converter imaging and numerical simulations of global subduction zones. Under significant trench retreat over the lifetime of a subduction zone, a mechanically 'soft' slab [*Li et al.*, 2008] could gradually settle at the base of the MTZ, as documented in the north–western Pacific subduction system. Dynamically, a dipping slab with a relatively low viscosity compared to the surrounding mantle tends to develop into a 'spoon' or 'jellyfish' shape with relatively smooth leading edges [*Loiselet et al.*, 2010] on top of a highly viscous lower mantle [*Quinteros et al.*, 2010; *Ribe et al.*, 2007]. The 'spoon' analogy is more consistent with the interpreted shape of the *660* in this study, where anomalous boundary variations extend well to the east of the Benioff zone. Slab stagnation near the base of upper mantle is a viable explanation. The easternmost segment of this broad zone appears to shallow toward mid–MTZ depths and may provide further evidence of a highly deformed slab in the MTZ due to thermal and/or compositional variations.

The distinctive reflection gap beneath the Brazil–Bolivia border remains enigmatic. Similar amplitude reduction have been documented near the Kurile–Japan arcs [*Gu et al.*, 2012] in connection with steep boundary topography in response to

substantial mass and heat fluxes across the *660*. While the reflection gap presented in this study is more distant from the Benioff zone than previously reported, waveform defocusing [*Chaljub and Tarantola*, 1997; *Gu et al.*, 2012] due to the interaction between the leading edge of the stagnant slab and the *660* offers a simple explanation. A potentially related structure is the strong reflector beneath the *660* reflection gap, which supports this interpretation and may result from avalanched oceanic lithosphere [*Tackley et al.*, 1993] near the same location. Delayed post–garnet transformation within the cold slab [*Kawakatsu and Niu*, 1994] or super–hydrous phase transitions in dense magnesium silicates occurring in hydrated crustal material [*Courtier and Revenaugh*, 2006; *Ohtani*, 2005; *Shieh et al.*, 1998; *van der Meijde et al.*, 2003, 2005] have been suggested as possible origins of lower mantle reflectors. On the other hand, the slab–centric interpretation of the aforementioned lower mantle reflector remains questionable for two key reasons: 1) relatively large data uncertainty in the vicinity of the *660* gap, and 2) consistent reflections at 800–950 km depth away from the Benioff zone, particularly beneath the Pacific ocean in the distance range of 0°–25°along profile. A chemical stratification [*Wen and Anderson*, 1997] cannot be ruled out as a viable explanation for the semi–continuous lower mantle interface at 800–950 km depth.

3.5 Conclusions

Our *SS* precursor analysis has revealed the stark contrast between the simple reflectivity structures in relatively undisturbed tectonic regimes and structure observed in regions of ongoing subduction. The *410* gap in the back arc of the Nazca subduction reveals what is likely a broad compositional anomaly at the top of the MTZ, although the specific mechanism for the observed reflectivity gap remains uncertain.

Additionally, the reflectivity anomalies observed near the base of the MTZ suggest structural complications of the subducting Nazca plate beyond a simple form of penetration. The Nazca slab likely undergoes significant deformation within the MTZ, resulting in pockets of stagnated lithospheric material at the base of the upper mantle. Finally, we identify anomalous reflectors beneath the Benioff zone. While this observation could be caused by subducted ocean lithosphere within the shallow lower mantle, laterally coherent reflectors identified in the depth range of 800–950 km, particularly beneath the Nazca plate, require further explanation.

Mapping the reflectivity structure beneath the craton–terrane transition in western Canada

4.1 Introduction

The North American continent, a very complex assemblage of disparate geological units, has undergone a significant periods of accretion, deformation, faulting, and rifting throughout its history. The ancient core of the continent, which consists of a number of Archean provinces, is among the oldest continental cratons in the world. It was formed prior to 2.0 Ga by the roughly coeval assembly of the Hearne, Superior, Rae, Slave, and Wyoming provinces[*Hoffman*, 1988; *Ross et al.*, 1991]. Following the collision of these former "micro–continents" to form ancestral North America, the continent was expanded by the Palaeoproterozoic accretion of several distinct oceanic terranes which now form much of the metamorphic basement rock that is

currently overlain by the Phanerozoic sedimentary cover of the Western Canadian Sedimentary Basin [*Hoffman*, 1988]. The most recent major period of westward expansion began in the Phanerozoic with the commencement of the subduction of the Kula and Farallon plates beneath the Pacific coast of North America resulting in the accretion of much of the the material now found in the Canadian Cordillera [*Harms and Evenchick*, 2007; *Hoffman*, 1988; *Ross et al.*, 1991]. The Juan de Fuca and Cocos plates, currently subducting beneath western Canada and central America respectively, are the last remnants of the former Farallon plate, with the bulk of the previously subducted material currently sinking into the lower mantle well to the east of the present–day continental margin [*Bunge and Grand*, 2000].

Previous research into the structure of the lithosphere and upper mantle beneath the Alberta Basin has come from a wide variety of sources. Teleseismic research began in earnest with the installation of the Canadian National Seismograph Network (CNSN) stations EDM and WALA the early 1990's, and early analysis of the data from these stations based on receiver function analysis [*Bostock*, 1996; *Cassidy*, 1995; *Eaton and Cassidy*, 1996; *Shragge et al.*, 2002] provided preliminary constraint on the differential delay times of the Moho, *410*, and *660* converted phases (referred to as *Pms*, *P410s*, and *P660s*, respectively). *Shragge et al.* [2002] utilized a similar dataset to investigate mantle structure using three separate methods of analysis: receiver function estimation, shear wave splitting, and body–wave tomography. Further additions to the dataset are provided largely through the Lithoprobe initiative [*Ross*, 2002; *Ross and Eaton*, 2002], with the deployment of the Canadian North–west Experiment (CANOE) [*Mercier et al.*, 2008], the BATHOLITHS project [*Mercier et al.*, 2009], and the Slave & Northern Cordillera Lithospheric Evolution (SNORCLE) transect, as well as several shallow refraction / reflection lines (e.g. the Alberta Basement Transect (ABT) [*Gorman et al.*, 2002],

and the Southern Alberta Refraction Experiment (SAREX) [*Clowes et al.*, 2002; *Gorman et al.*, 2002]). These projects vary from crustal investigations using shallow active–source reflected and refracted waves [*Clowes et al.*, 2002; *Gorman et al.*, 2002] to approaches such as ambient–noise tomography [*Dalton et al.*, 2011]. On a broader scale, a recent receiver function analysis by *Thompson et al.* [2011] on array data has suggested that the Mantle Transition Zone (MTZ), a region bounded by the 410 km and 660 km discontinuities, is relatively unperturbed either thermally or chemically beneath much of continental North America.

Information regarding velocity variations in the mantle beneath western Canada has been provided by both global [*Bijward et al.*, 1998; *Grand*, 1994, 2002; *Grand and Helmberger*, 1984; *Montelli et al.*, 2004; *Obayashi et al.*, 2006; *Ritsema et al.*, 2004; *Simmons et al.*, 2010] and regional [*Frederiksen et al.*, 2001; *Grand*, 1994; *Grand et al.*, 1997; *Nettles and Dziewonski*, 2008; *Shragge et al.*, 2002; *van der Lee and Nolet*, 1997] tomographic inversions that generally reveal a sharp east–west velocity gradient near the Cordilleran Deformation Front. This gradient marks the boundary between a region of hot mantle material beneath the Cordillera, caused by subduction related shallow mantle flow [*Currie and Hyndman*, 2006] and the relatively cool mantle that underlies the craton [*Blum and Shen*, 2004]. The depth extent of this sharp transition varies between models; however, it generally remains confined to the upper mantle, leading to interpretation as a transition from the high velocity lithosphere that makes up the ancestral craton and the low velocities corresponding to the mantle beneath the Cordillera.

The presence of thermal and chemical anomalies in the MTZ and upper mantle, would, if detected, tell us much regarding the past history of subduction in the region. Anomalies at transition zone depths may be present in this region, perhaps due to the lingering effects of the Farallon slab on the surrounding mantle, or ongoing effects

from the active subduction of the Juan de Fuca plate at the Cascadia subduction zone. Both the *410*, arising from the phase transition of olivine into the higher–pressure polymorph wadsleyite, and the *660*, formed through the pressure–induced decomposition of another olivine variant (ringwoodite), into Mg–perovskite and magnesiowustite [*Bina*, 2003; *Helffrich*, 2000; *Ita and Stixrude*, 1992; *Katsura and Ito*, 1989; *Katsura et al.*, 2004], have been found to provide accurate constraint on the temperature and mineralogy of the surrounding mantle [*Shearer and Masters*, 1992] due to the depth variability of these phase transitions upon encountering thermal and chemical heterogeneity. The delay times of the P–to–S conversions arising from crust and mantle interfaces (referred to as Pds phases, where d denotes the depth of the converting interface) are a proven high–resolution means of resolving the depths of the MTZ discontinuities.

This study presents an investigation of the MTZ and upper mantle structure beneath the Canadian Rockies and Alberta Network (CRANE) of seismic stations situated near the margin of the North American craton (see fig. 4.1). Utilizing radial receiver functions [*Ammon*, 1991; *Cassidy*, 1992; *Langston*, 1979; *Ligorria and Ammon*, 1999] computed from data collected over the past 6 years of the array deployment, we are able to obtain measurements of the depths of the 410 and 660 km seismic discontinuities. Singular Spectrum Analysis (SSA) [*Cadzow*, 1988; *Oropeza and Sacchi*, 2009; *Sacchi and Ulrych*, 1995; *Trickett*, 2003] is applied to individual station gathers for noise attenuation and interpolation of irregularly spaced data, and the least–squares parabolic Radon transform [*Sacchi and Ulrych*, 1995; *Schultz and Gu*, 2012] for improved detection of the $P410s$ and $P660s$ peaks in the $\tau - p$ domain. The combination of these two algorithms allows the measurement of MTZ conversions for stations with higher noise levels and fewer available traces than previous approaches.
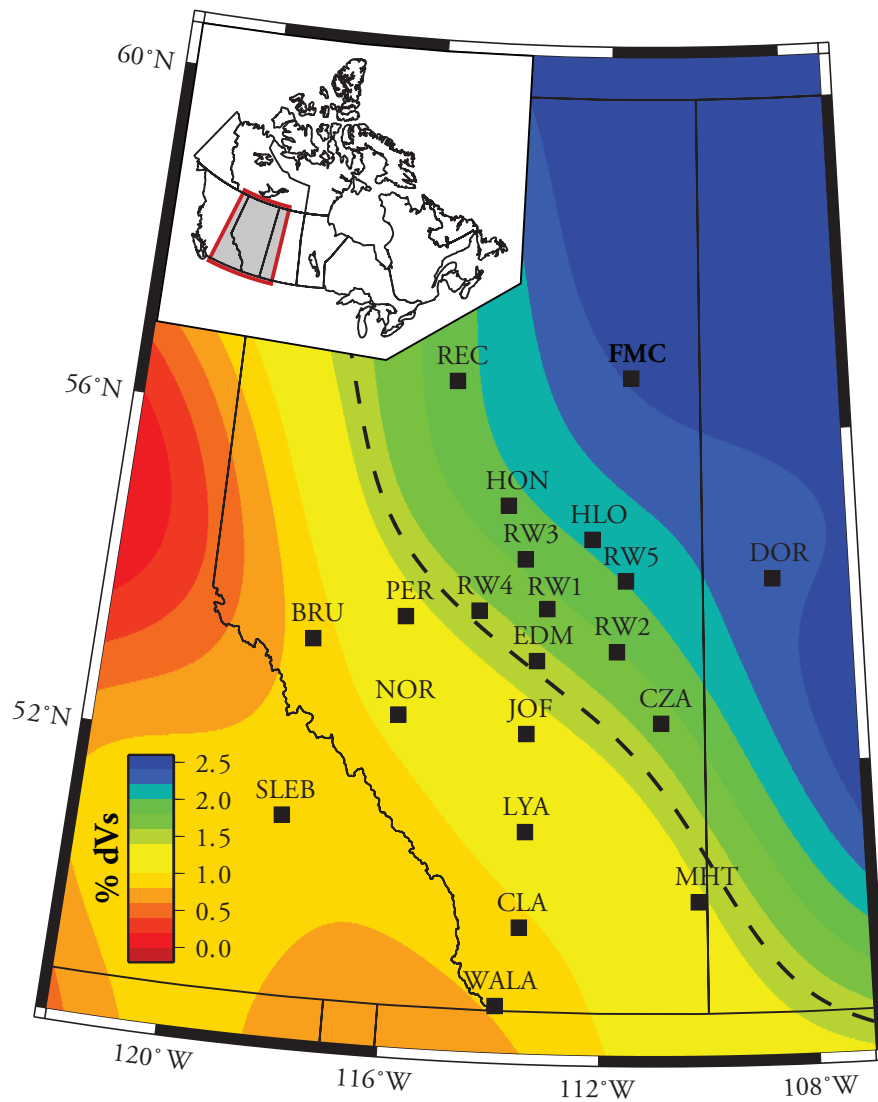
Figure 4.1: Seismic stations of the CRANE array and the CNSN stations EDM, WALA, and SLEB. Station locations are superimposed on a 50 km slice through the ND2008 shear velocity model [*Nettles and Dziewonski*, 2008], with the +1.5% contour shown as a dashed black line representing the approximate boundary of the Rocky Mountain Deformation Front.

4.2 Data and Methodology

Eighteen broadband, three–component seismic stations from CRANE greatly improves the regional coverage of teleseismic and local earthquakes in Western Canada (see Figure 4.2). This semi–permanent network [*Gu et al.*, 2011] was designed to complement the existing receivers at Edmonton (EDM), Waterton Lake (WALA), and Sale Mountain (SLEB), three permanent broadband stations that began operating in the early 1990s as a part of the Canadian National Seismograph Network. The combination of these two arrays provides nearly uniform coverage beneath the southern Western Canadian Sedimentary Basin (WCSB) with an average distance of ~150 km between stations. The main imaging approach used in this study is an improved analysis based on the receiver function technique [*Ammon*, 1991; *Bostock*, 1996; *Cassidy*, 1995; *Gu et al.*, 2011; *Langston*, 1977; *Ligorria and Ammon*, 1999; *Liu et al.*, 2003; *Tauzin et al.*, 2008; *Vinnik*, 1977]. The short–period nature of receiver functions computed from P–to–S converted waves enables high resolution constraints on the depth and impedance (the product of density and velocity) contrast of crustal and mantle interfaces beneath a given seismic station (see *Rondenay* [2009] for review). By taking advantage of this approach and the waveforms from the CRANE and CNSN stations, we are able to interrogate the mantle at significantly higher resolution than earlier studies in this region. Below is a detailed account of the data and imaging methodology.

4.2.1 Preprocessing

Our dataset begins with over 8800 earthquakes with moment magnitudes greater than 5.5. All events occurred during the years of 1992–2011 (with 2006 being the first year containing CRANE data) at distances of 30°to 90°from the receivers

(Figure 4.3a), an ideal range for receiver function analysis [*Langston*, 1977; *Rondenay*, 2009; *Vinnik*, 1977] due to the near–vertical incidence angle of the P–wave ray–paths. After rotating the original components to vertical, radial and transverse, we remove the mean and linear trend and apply a Hanning taper to the edges of each trace. The seismograms are subsequently integrated to displacement and Butterworth band–pass filtered with corner frequencies at 0.07 Hz and 1 Hz. This frequency range was empirically chosen through experimentation to maximize the visible energy in the expected arrival window of the 410 and 660 km converted phases, the main focus of this study, as well as to minimize incoherent noise. We then compute the standard deviation of the vertical component seismogram in the time window of 1 – 25 sec after the predicted P–wave arrival time based on PREM [*Dziewoński and Anderson*, 1981]. The ratio between this value and that of the noise window, which is similarly defined for the time window of 105–5 sec prior to P, is used as the signal–to–noise ratio (SNR) criterion to eliminate noisy records; event–station pairs with SNR less than 2 are automatically removed from further consideration. This procedure retains 4846 (55% of the original data) high–quality event–station pairs for the analysis of receiver functions. The resulting distribution of back–azimuths (Figure 4.3b) reveals dense coverage in relatively narrow azimuthal ranges, primarily centred around 285°– 320°and 135°– 160°. This limited range precludes a comprehensive analysis of back–azimuth dependent effects at most of the stations.

4.2.2 Receiver Function Estimation

The iterative deconvolution technique of *Ligorria and Ammon* [1999] is then applied to the selected radial and vertical component data traces. The deconvolution of the vertical from the radial component, which effectively removes the source effects and isolates the converted S–wave arrivals, adopts a Gaussian filter width of 0.8

(e.g., *Crotwell and Owens* [2005]) to maximize the coherence and visibility of the MTZ conversions *P410s* and *P660s*. Up to 500 iterations are performed during the time–domain inversions to ensure the convergence of the solutions, while a minimum 0.0075% data fit improvement is imposed on each additional spike as the stopping criterion. This fit improvement criterion is small enough that, for the vast majority of the cases, the maximum number of peaks is inserted into the receiver function. We permit both positive and negative phases to be added to the deconvolved receiver function. The data misfit and percentage match (Figure 4.4) to the original data allow further winnowing of the dataset as receiver functions with a data–fit percentage below 80% are automatically rejected. This procedure places a greater emphasizes the quality of the converted phases (rather than the dominant P phase) and a total of 1790 high–quality receiver functions are retained for the final analysis.

4.2.3 Crust and Mantle Heterogeneity Corrections

To minimize the effects associated with crustal thickness and composition, we compute travel time corrections using the CRUST2.0 [*Bassin and Laske*, 2000]; the choice of a global model is necessitated by the limited published constraints on crustal depth from regional data. For each event–station pair, travel times are computed by integrating the unperturbed geometrical ray path between piercing points of the *P* and *Pds* phases at the model Moho depth beneath the station for both the heterogeneous model and PREM; the difference between these two values is subsequently applied to the corresponding receiver function as a time shift. The effect of upper mantle heterogeneity above the *410* is also minimized by tracing rays through layered shear velocities from ND2008 [*Nettles and Dziewonski*, 2008] and scaled P velocities computed from the same model using the *P/S* velocity ratio of PREM [*Dziewoński and Anderson*, 1981]. Figure 4.5 shows histograms of the

Alberta Yearly Recorded Event-Station Pairs
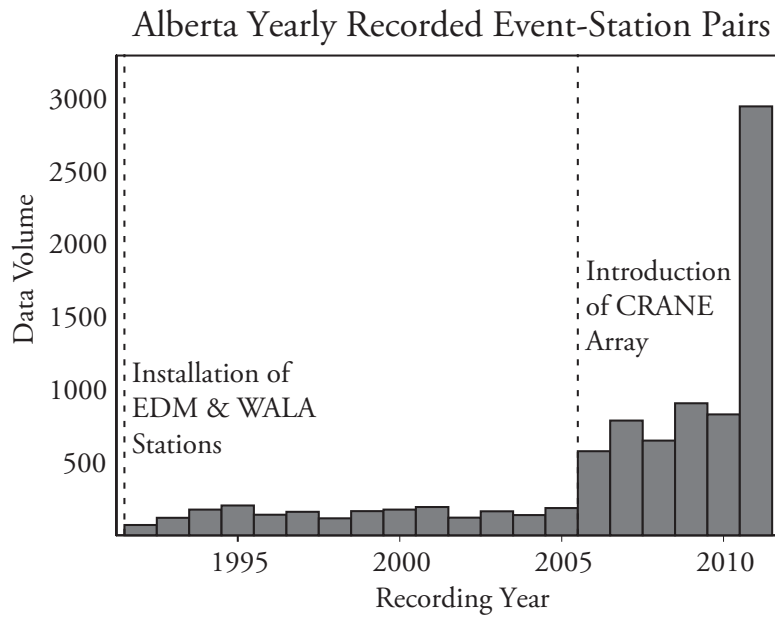
Figure 4.2: Teleseismic data volume recorded within Alberta by the CNSN and CRANE arrays, by year.
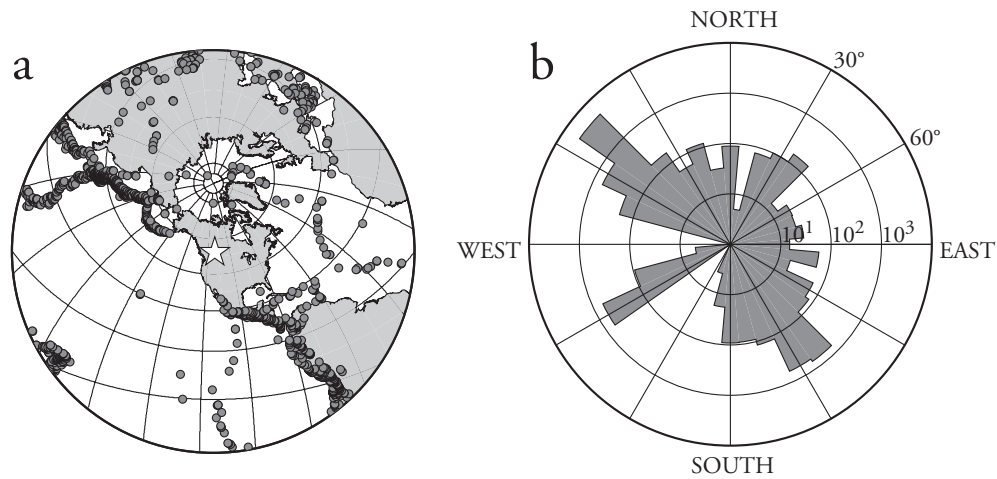
Figure 4.3: a) Epicentre locations (grey circles) for all events used in this study. Location of the CRANE Array marked with a star b) Back–azimuth rose plot of the entire receiver function dataset, shown using a logarithmic scale for the petal length.
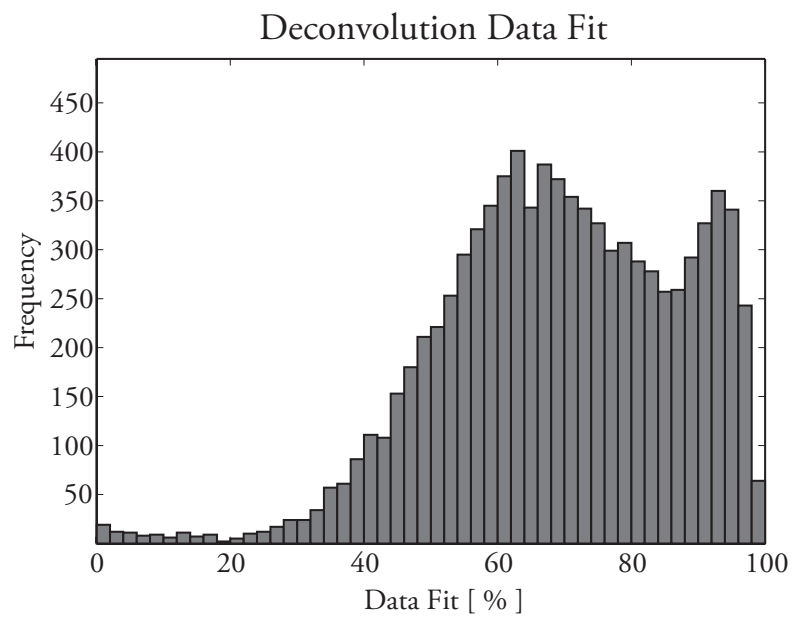
Figure 4.4: Percentage data fit histogram for the receiver function dataset after time–domain iterative deconvolution.

crustal correction (Figure 4.5a), heterogeneity correction (Figure 4.5b), and the total correction (Figure 4.5c). The thickest crust, hence the largest negative correction, lies beneath the foreland belt of the Northern Rockies. The average thickness difference between the foothills of the Rockies (BRU, NOR, SLEB, WALA) and the Alberta Basin is ~10 km. To quantify the effect of varying crustal thickness on the observed depth of the MTZ discontinuities, we perform a hypothesis test by 'stretching' the CRUST5.1 model to increase the total thickness by 10 km, and re–compute the correction for a reference distance of 60 deg. The resulting crustal correction changes from the reported value (see Table 4.1) by an average of 0.16s for every 10 km of change in the crustal thickness; this would translate to a shift of ~2 km in the depth of the 410. The crustal effect is counteracted by the positive influences from the cold cratonic lithosphere in the ND2008 model, although the overall correction (see Figure 4.5) is generally negative due to the differences in the strength of the corrections. The net effect of a negative correction is a reduction in the converted phase arrival time relative to P, which results in deeper interfaces.

4.2.4 Partial Stacking and Singular Spectrum Analysis

In theory, signals from a single receiver function are capable of constraining the depths of crust and mantle interfaces adequately. In practice, however, measurements based on secondary conversions are often unreliable due to the presence of random noise, scattering and/or interfering phases. Signal enhancement is vital in this study due to the low overall SNR at temporary seismic stations, mainly resulting from the thick Phanerozoic cover in southern WCSB. Several steps were taken to enhance the SNR, beginning with a 'partial stacking' procedure that performs a running average of receiver functions at each station based on epicentral distance (see also sections below). The default averaging window size (or, bin width) is 1°, which is heuristically
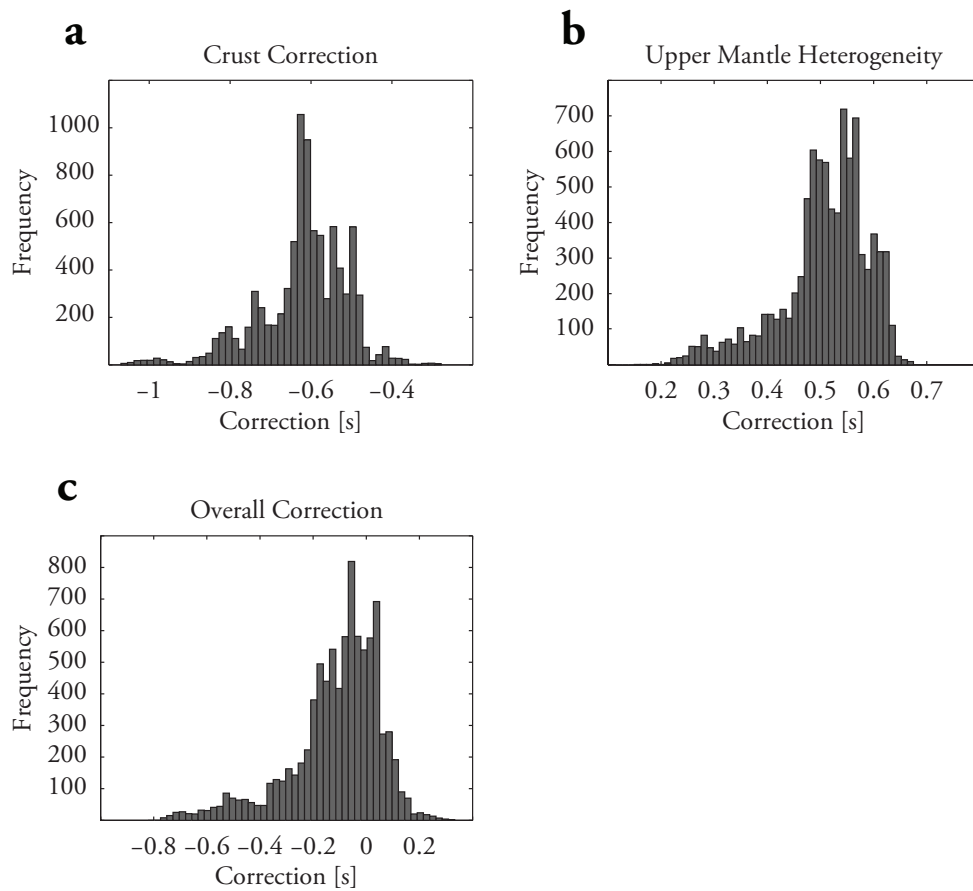
Figure 4.5: Histograms of the corrections applied to the receiver function dataset. a) Crustal correction using CRUST5.1 [*Mooney et al.*, 1998]. b) Mantle heterogeneity correction using the ND2008 shear velocity model [*Nettles and Dziewonski*, 2008] c) Total correction, sum of a and b

determined to balance the needs of data resolution and noise reduction; despite significant variations in data volume, this value ensures that all stations finished with less than 36% empty averaging bins. Figure 4.6a shows the partial stack of the entire dataset prior to further de–noising. The amplitudes of key signals of interest (e.g., the *410* and *660*) are improved by more than 3x in the regional gather.

Singular Spectrum Analysis (SSA) is subsequently applied to simultaneously remove gaps in the gathers and de–noise the individual data traces. The SSA method (also referred to as Cadzow filtering) [*Cadzow*, 1988; *Oropeza and Sacchi*, 2009; *Sacchi and Ulrych*, 1995; *Trickett*, 2003] operates in the frequency–space (f–x) domain on a frequency–by–frequency basis via SVD factorization to reduce the rank of Hankel matrices containing spatial vectors from the f–x domain data. SSA is employed as part of an iterative partial–reconstruction approach (described in more detail in Section 2.3) to de–noise and interpolate the partially stacked receiver functions. We apply the SSA approach to the individual station data as well as to the dataset as a whole, preserving the five most significant singular values while maintaining 40% of the original data through eight iterations of partial reconstruction.

4.2.5 Least–Squares Parabolic Radon Transform, Stacking, and Depth Conversion

Time–space domain data gathers after partial stacking, de–noising and interpolation are subjected to the least–squares Parabolic Radon Transform (PRT) for reliable, simultaneous constraint on the ray parameters and arrival times of secondary converted phases. The PRT is an integral transform that, similar to slowness slant–stacking and vespagram summation [*An et al.*, 2007; *Gu and Sacchi*, 2009; *Rost and Thomas*, 2009], projects data in the spatial time and offset (t, Δ) domain onto the Radon (reduced time τ, ray parameter p) domain. When posed as a least–squares inverse
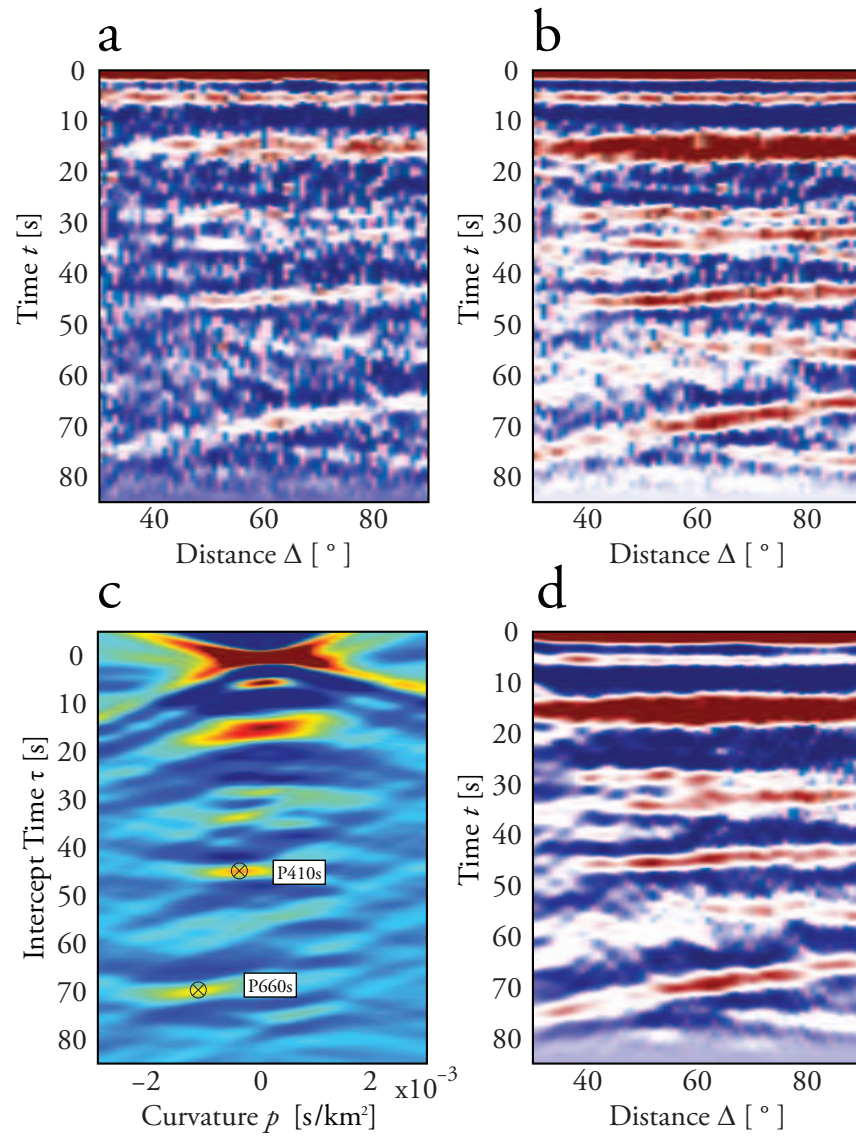
Figure 4.6: a) Noisy partially–stacked seismogram data. b) De–noised data following application of SSA. c) Least–squares parabolic Radon transform of de–noised data. The symbols mark the location of the peaks of the *P410s* and *P660s* phases. d) Data reconstructed from Radon panel.

problem involving individual frequency components and proper regularization [*Schultz and Gu*, 2012], the PRT (and the Radon Transform in general) can be a reliable high–resolution tool for signal detection and isolation.

Because a single damping parameter is applied to the PRT least–squares inversion, we mute the direct P and Moho conversion/multiple phases, arrivals that dominate the data fit, prior to the application to improve the recovery of smaller, secondary phases. The muted traces subsequently undergo the PRT [*An et al.*, 2007; *Beylkin*, 1987; *Sacchi*, 1997; *Sacchi and Ulrych*, 1995] with a reference distance of 60°and an empirically determined regularization parameter μ based on the variable noise level at each station. Stations with higher average noise levels (or lower overall signal quality) are damped more severely for reliable solutions.

To determine the depth of the MTZ arrivals for each individual station, the 20 most significant local and global maxima in the Radon domain are identified and compared to the results of the regional average stack. The two peaks closest to the regional values for *P410s* and *P660s* are designated as the signal of interest. The resulting values for arrival time, discontinuity depth, and the corresponding uncertainty are recorded in Table 4.1. The Radon domain images are reviewed manually, and stations with inconclusive Radon domain signals are excluded from the interpretations.

As the final step, we construct a stacked summary trace for each station in the dataset (Figure 4.9) and for the entire array combining CRANE and CNSN stations. The crust– and depth–corrected data traces are converted to depth using PREM [*Dziewoński and Anderson*, 1981], and the resulting depth–domain data are linearly stacked to provide a secondary constraint on the quality of the MTZ arrivals. The standard deviation is computed for each depth sample and shown in Figure 4.7; this figure demonstrates the strong consistency between the depth stacks and the

Table 4.1: CRANE MTZ Measurements

Sta	Lat	Lon	*P410s*	*410*	+/-	*P660s*	*660*	+/-	Cor	Fold
–	[°]	[°]	[s]	[km]	[km]	[s]	[km]	[km]	[s]	–
Overall	–	–	44.6	419.0	6	69.4	671.1	8	-0.173	1900
BRU	53.3	-117.9	45.2	424.9	11	69.6	673.3	24	-0.226	46
CLA	50.0	-113.5	45.0	422.9	9	70.0	677.8	7	-0.071	41
CZA	52.5	-110.9	44.6	419.0	6	68.6	662.7	8	-0.135	100
DOR	54.2	-108.6	–	415*	–	–	669*	–	-0.127	12
EDM	53.2	-113.4	44.0	413.2	7	68.0	656.4	14	-0.147	434
FMC	56.7	-111.5	–	417*	–	–	661*	–	-0.008	29
HON	55.1	-114.1	–	421*	–	–	665	–	-0.016	27
JOF	52.3	-113.5	–	415*	–	–	658*	–	-0.106	15
LYA	51.2	-113.5	42.6	399.7	8	69.0	666.9	14	-0.157	47
NOR	52.5	-116.1	45.4	426.8	9	69.2	669.0	8	-0.195	114
PER	53.7	-116.0	45.6	428.8	8	69.8	675.6	8	-0.239	139
RW3	54.4	-113.7	–	404*	–	–	665*	–	-0.099	18
RW4	53.8	-114.6	–	413*	–	–	659*	–	-0.034	13
SLEB	51.2	-118.1	44.8	421.0	6	69.8	675.6	11	-0.367	297
WALA	49.1	-113.9	45.0	422.9	7	70.4	682.3	15	-0.114	479

Recording station locations, MTZ converted-phase delay times *P410s* and *P660s*, and their corresponding depths. Empty cells indicate stations where depth measurements were made directly from summary traces rather than from the Radon panel. These depths are also denoted with an asterisk (*).

corresponding PRT images.

4.3 Results

The depths of the 410 and 660 km discontinuities beneath individual CRANE and selected CNSN stations are determined based on the outcomes of the procedures outlined in Chapter 2. In addition, receiver functions from all stations are combined to form a single dataset and subjected to the same procedures to provide a relatively unbiased regional average (see Table 4.1 for values). The result of regional averaging leads to robust mantle conversion measurements, thanks to the substantial data volume resulting in the *P410s* and *P660s* arrivals peaking well above the background noise level (see Figure 4.7). The inverted Radon signals from individual station gathers are less stable, as only 10 out of 21 stations exhibited mantle conversion arrivals significantly above the background noise level (Figure 4.8). It is worth noting that improvements in the clarity of converted phases based on partial stacking and SSA reconstruction are strongly dependent on data volume; stations with limited data tend to remain inconclusive, whereas stations with qualitatively high signal coherency prior to PRT inversion appear to improve considerably. The modelled data from the PRT forward operation (Figure 4.6d) shows a high degree of correspondence to the input data, further increasing confidence in the results. Of the 11 stations with low signal strength and coherence, the majority have been deployed relatively recently (2010–2011, especially RWA stations near EDM) and the results at these locations are expected to improve over the next few years. The nonlinear move–out curves for both *P410s* and *P660s* are clearly visible in both the input and modelled data gathers. Due to higher recorded data volume and superior vault construction, the three permanent stations (EDM, WALA, SLEB) consistently show slightly higher
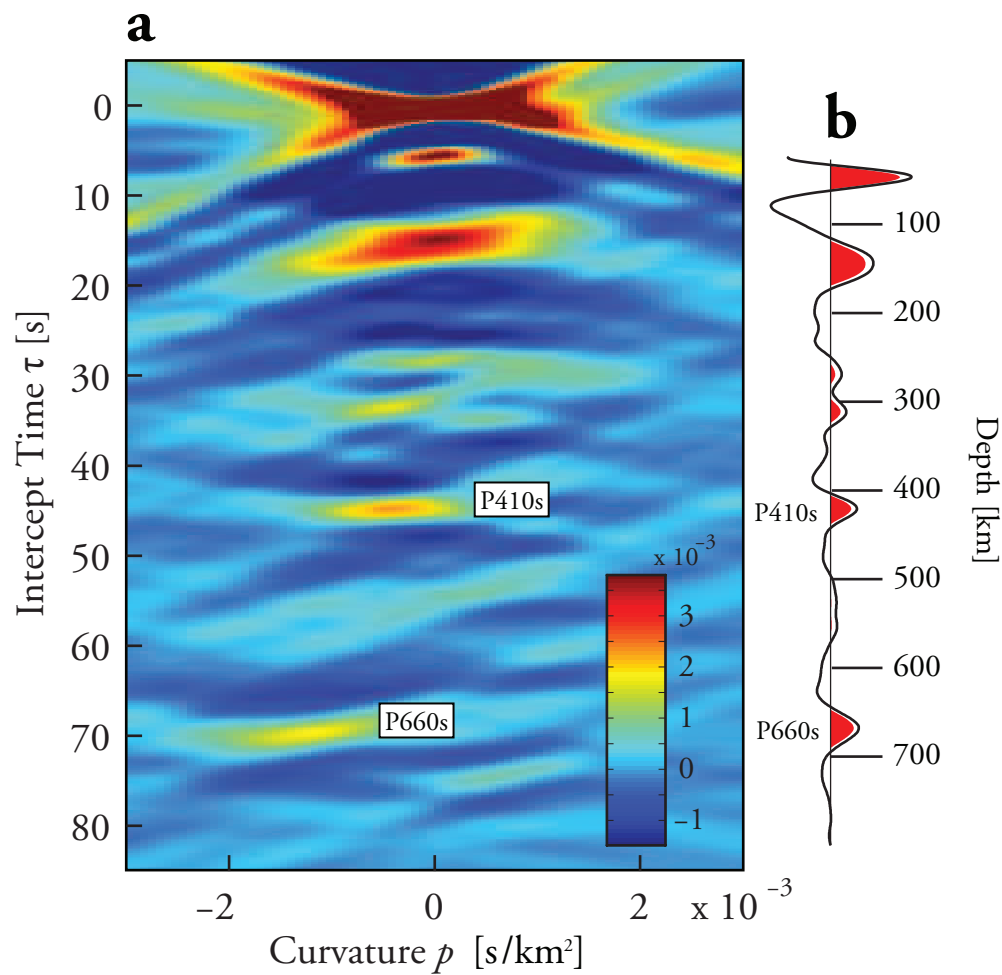
Figure 4.7: a) Least–squares PRT transform of the entire dataset. The labels indicate the peaks of the converted phases *P410s* and *P660s*. b) Stacked summary trace of the entire dataset. The *P410s* and *P660s* peaks are clearly visible at the same depth as the energy in a).

SNR than the regional average (for example see Figure 4.8a,c vs. Figure 4.8b,d).

From the regional Radon solution (Figure 4.7) we obtain average MTZ discontinuity depths of 419.0 km and 671.1 km for the *410* and *660*, both of which are deeper than the respective global averages of 409–410 km and 650–660 km [*Deuss and Woodhouse*, 2002; *Gu et al.*, 2003; *Houser et al.*, 2008]. The resulting MTZ thickness is 254.3 km, which is approximately 10 km thicker than the global average [*Flanagan and Shearer*, 1998; *Lawrence and Shearer*, 2006; *Tauzin et al.*, 2008]. The Radon–based measurements are reasonably consistent with the values measured directly from the time–domain summary trace (at 419 km and 665 km, respectively). A slightly thick MTZ (by ~8 km) in the PRT estimate translates to a modest temperature decrease of 31°C, assuming a vertical structure that affects both the olivine $\rightarrow$ wadsleyite and ringwoodite $\rightarrow$ perovskite + magnesiowustite transitions. Furthermore, the Radon–domain amplitude of the *660* peak is 76.5% of that of the *410*. This ratio is consistent with the average ratio of individual stations (80.5%) as well as with time–domain average amplitude ratio on the receiver functions (0.86).

The depth of the *410* at individual stations ranges from 399.7 km at LYA to 428.8 km at PER, a 29 km difference. The range of the *660* is 26 km, bounded by the minimum value of 656.4 km beneath EDM and the deepest interface at 682.3 beneath WALA. Assuming a purely thermal origin, it is possible to translate these values into temperature anomalies at the discontinuity depth. In doing this, we search for sites where the depth measurements indicate a consistent thermal anomaly at both 410 and 660 km. Without this constraint, the depth variability across the array produces unrealistic scenarios. Two stations satisfy this requirement: EDM and LYA, with thermal anomalies of +57°K and -123.6°K, respectively.

Variations in discontinuity depths are generally well constrained. In all cases,
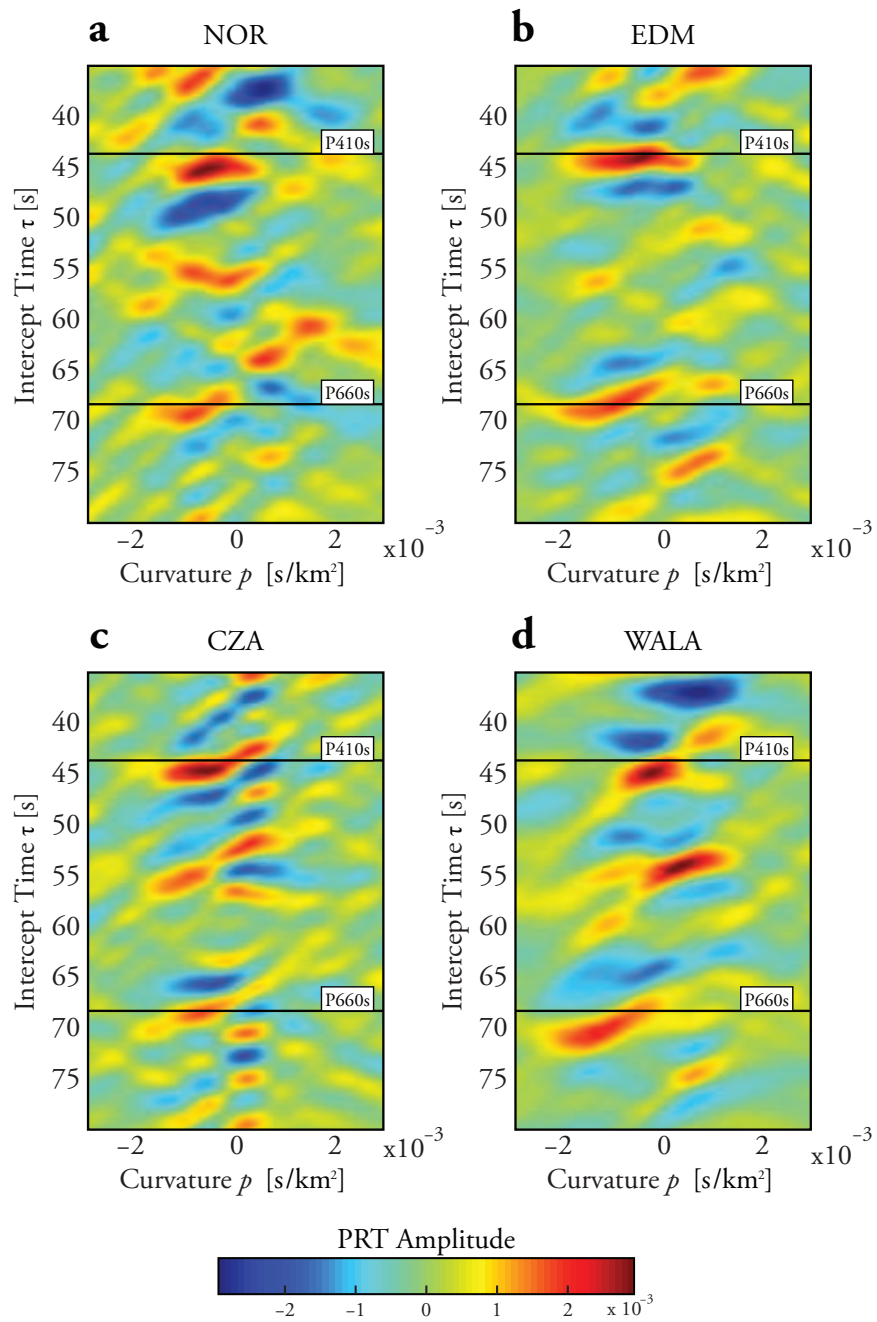
Figure 4.8: Radon panels from four individual stations. The PREM–predicted arrival times of the *P410s* and *P660s* phases are marked by the black lines. a) Nordegg, AB (NOR) b) Edmonton, AB (EDM) c) Czar, AB (CZA) d) Waterton Lake, AB (WALA)
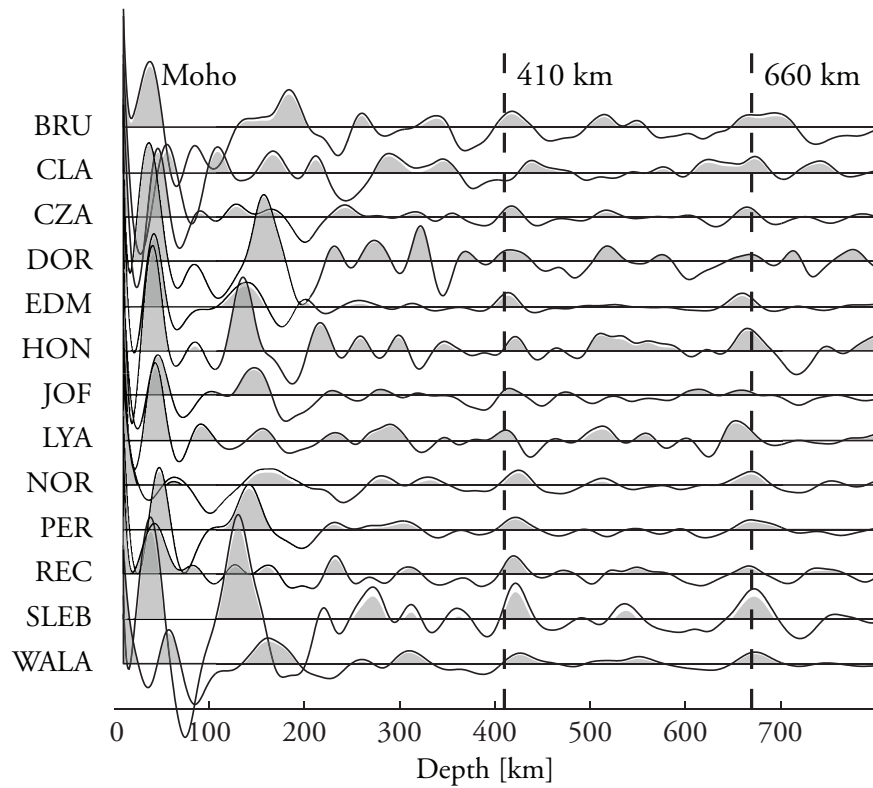
Figure 4.9: Stacked, depth–converted receiver functions for the stations used in the study. The black line is the summary trace, while the grey fill indicates the positive energy above 2 standard deviations. The depths of the *410* and *660* are marked with dashed lines. The large–amplitude pulse immediately following the direct P is the Moho conversion.

the elliptical shapes of the Radon signals suggest greater resolutions along the time (or depth) axis. Using a subjective amplitude of 75% (relative to the peak amplitude), we estimate the depth uncertainties to be 8 and 10 km for the regionally averaged *410* and *660*, respectively (Table 4.1). These values are considerably larger, but potentially more realistic, than those of earlier studies with values on the order of 2–5 km (e.g., [*Flanagan and Shearer*, 1998; *Gu et al.*, 1998; *Lawrence and Shearer*, 2006, 2008; *Tauzin et al.*, 2008])

We fail to observe energetic arrivals in the vicinity of the 520 km discontinuity in the region–wide Radon solution. Mid MTZ discontinuities are known to be weak [*Gu et al.*, 1998] or complex [*Deuss and Woodhouse*, 2002] 2002) beneath major continents and, in this case, the effect of averaging may also play a role. While the summary amplitude is below the 2σ limit, one or multiple peaks can be identified on ~50% of the receiver functions from individual stations (see CZA for instance, Figure 4.8c). Interpretations of these intermittent signals require careful future work, as a positive parameter of curvature (rather than an expected negative one for *520*) is sometimes observed.

One method to avoid uncertainty and ambiguity in the interpretation of MTZ converted wave arrivals is to view the differential *P660s–P410s*, or MTZ thickness. This quantity is relatively insensitive to the structure above the *410* due to the cancellation of common *P410s* and *P660s* ray segments beneath a given station. Figure 4.10c shows the computed MTZ thickness values across the array. A distinct north–south zonation is clearly visible, showing an MTZ thickness of 243 km beneath the northern stations (EDM, PER, BRU, NOR, and CZA) and 258 km beneath the southern stations. The thickest MTZ (~266 km) is observed under station LYA, and its exclusion leads to a reduced (southern) average of 255 km. The width of the MTZ beneath northern–central Alberta is comparable to global averages

from *SS* precursors (242 km [*Flanagan and Shearer*, 1998; *Gu and Dziewoński*, 2002]) and *P*-to-*S* conversions [*Lawrence and Shearer*, 2006; *Tauzin et al.*, 2008], which could suggest limited perturbations in temperature or composition relative to the global average. On the other hand, the MTZ width in southern Alberta is nearly 15 km thicker than its northern counterpart and more closely resembles the subduction zone average of global and regional subduction zones (see Section 4.4). Figure 4.10d shows the MTZ thickness corrections based on ray tracing through ND2008, superimposed on the model shear velocities at 500 km. The corrections applied to the MTZ thickness values follow a similar trend to the heterogeneity slice, as would be expected from the long wavelength nature of the tomographic inversions. All values are negative due to the large–scale slow velocity anomaly at mid MTZ depths in ND2008; however the magnitude of the correction increases to the northeast, approximately along the gradient of the velocity anomaly. Once the travel time corrections are converted into depth, we find that the average correction values (mean of 0.41 s) correspond to less than 5 km of thickness adjustment. This slight correction does not completely eliminate the zonal pattern nor the anomalously thick MTZ beneath the southern stations (Figure 4.10c).

The contrast between our values and the results obtained by global studies is highlighted in Figure 4.11. The depths of the *410* and *660* are plotted against one another to facilitate comparisons of the results of different methodologies and data–sets. Superimposed on the plot is a curve of the hypothetical *410* and *660* depths under variable temperature regimes, calculated using the experimentally determined Clapeyron slopes of the olivine to wadsleyite (+3.2 MPa/°K [*Helffrich*, 2000]) and ringwoodite to magnesiowustite & perovskite (-2.0 MPa/°K [*Helffrich*, 2000]) phase transformations and a geopressure gradient computed using PREM layer densities. The results taken from global *SS* precursor studies [*Gu et al.*, 2003;
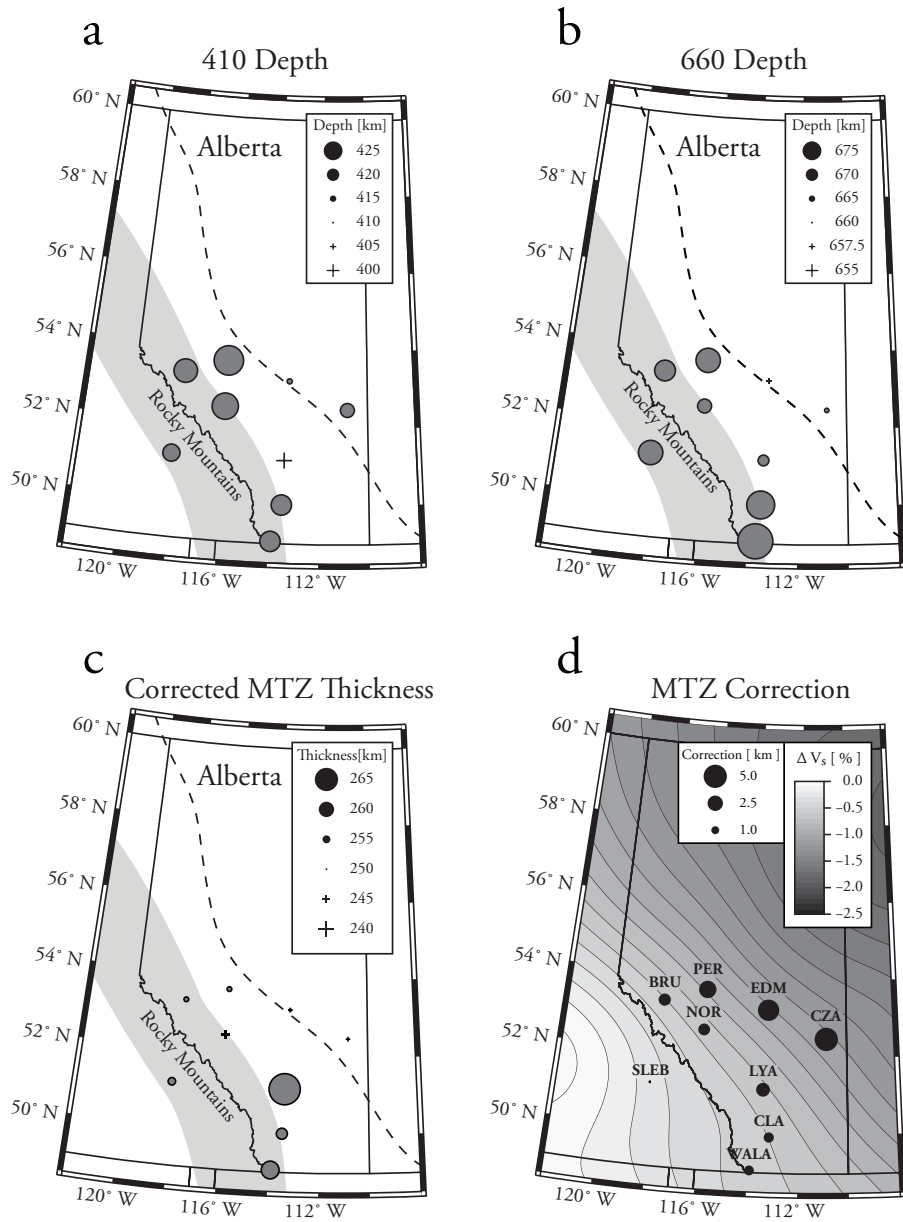
Figure 4.10: MTZ depth and thickness results taken from the PRT of individual stations gathers. The shaded grey region represents the Rocky Mountain chain. The dashed black line is the +1.5% shear velocity contour from model ND2008 at 50 km, indicating the approximated edge of the craton. Filled circles show values greater than average, with crosses marking locations where results where below average. a) Depth of the *410*. b) Depth of the *660*. c) MTZ thickness from the discontinuity depths. d) Crosses show the MTZ heterogeneity correction applied to account for structure between 410 km and 660 km. The background shows the shear velocity perturbation at 500 km in model ND2008.

Houser et al., 2008] are clustered primarily in the lower quadrants of the crossplot (corresponding to a shallow *660*), while our values and the results obtained through earlier receiver function analyses [*Bostock*, 1996; *Tauzin et al.*, 2008] mainly reside in the upper right–hand quadrant of the figure. This observation likely result from differences in imaging scale between *SS* and RF methodologies, where substantial local–scale variations possibly associated with young accreted terranes may have been largely averaged out by the former approach.

4.4 Discussion

4.4.1 General Assessment

Recent studies of the structure of the MTZ beneath the northeastern Canadian portion of the North American craton have revealed a simple MTZ relatively unmodified by thermal or compositional variations in the upper mantle [*Bostock*, 1996; *Thompson et al.*, 2011]. By analyzing receiver functions from a dense regional array in and around the Hudson Bay, *Thompson et al.* [2011] show that both MTZ discontinuities are elevated beneath the craton but deepen slightly towards the margins. The thickness of the MTZ remains roughly constant, which is interpreted as evidence of a 'flat' MTZ [*Thompson et al.*, 2011] beneath the cratonic interior, although considerably northeast of our study region. In comparison, the mantle reflectivity variations west of the study region are considerably more complex, as evidence from long-period analysis of global *SS* [*Flanagan and Shearer*, 1998; *Gu et al.*, 1998, 2003], *PP* precursors [*Chambers et al.*, 2005; *Deuss*, 2009] and intermediate–period receiver functions [*Lawrence and Shearer*, 2006] have generally suggested decreases in MTZ thickness in response to high upper mantle temperatures beneath the Pacific ocean basin. The interplay between the broadly averaged low velocity zone and more

MTZ Discontinuity Deflection
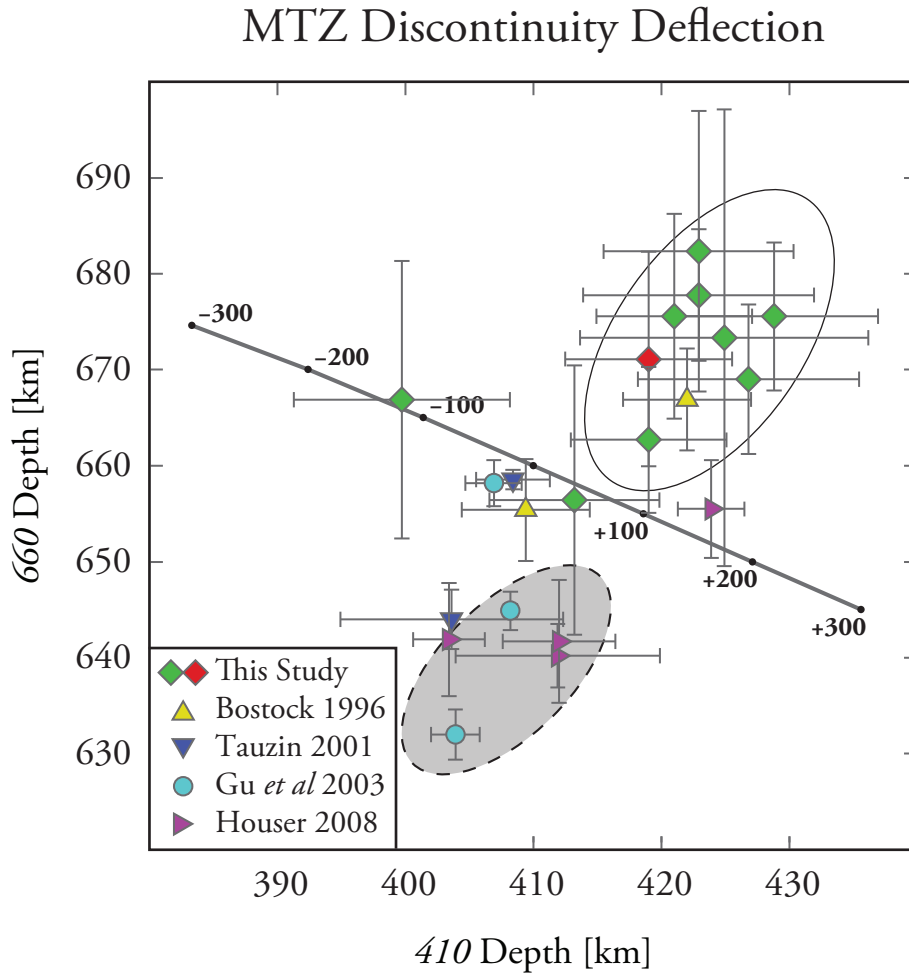
Figure 4.11: Crossplot of the values for *410* and *660* in the study region, from various studies. Green diamonds are the individual values from this study, with the red diamond indicating the results found for the region as a whole. Yellow triangles are results for stations EDM and WALA from the Pds study of *Bostock* [1996]. Blue inverted triangles are results for stations FFC (Fort Churchill, MB) and LLLB (Lilloet, BC) from the Pds study of *Tauzin et al.* [2008]. Cyan circles and magenta arrows are results from global SS studies, performed by *Gu et al.* [2003] and *Houser et al.* [2008], respectively. The shaded, dashed grey oval shows the region of the plot populated primarily by results from low resolution global studies, with the solid oval shows the regions where the results from our study congregate. The thick grey line shows the theoretical values for the *410* and *660*, for a constant temperature anomaly affecting both boundaries. The Clapeyron slopes for the *410* and *660* are taken from *Helffrich* [2000].

localized thermal structures, e.g., thin low-velocity layer above the *410* and high velocity slab structures [*Schaeffer and Bostock*, 2010] within the descending Juan de Fuca plate, highlights the complex seismic structures and layering west of our study region. The mantle reflectivity structure in the Cordillera and the Alberta Basin remain largely unknown. While global discontinuity maps (e.g., *Flanagan and Shearer* [1998]; *Gu et al.* [2003]; *Lawrence and Shearer* [2008]) indicate a relatively flat MTZ, reductions in discontinuity topography are expected due to the averaging effects associated with large Fresnel zones [*Neele et al.*, 1997]. The use of higher–resolution approaches such as receiver functions was previously limited to sparsely populated national network stations [*Bostock*, 1996; *Cassidy*, 1995], linear temporary arrays [*Courtier et al.*, 2006; *Shragge et al.*, 2002], or crustal scale investigations [*Bostock et al.*, 2010; *Cassidy*, 1995; *Clowes et al.*, 2002].

The stations used in this array help to bridge the gap in data coverage, from which the receiver function data shed new light on the craton-terrane transition in southwestern Canada. In contrast to eastern Canada, the mantle structure and stratification above and within the MTZ are highly variable in a relatively confined region between the Alberta basin and Rocky Mountain foreland belt. Both the *410* and *660* are strongly depressed, which far exceeds the level of perturbations from previous global estimates. The apparent topographic correlation between these two boundaries cannot be fully accommodated by a through-going thermal anomaly within the MTZ [*Deuss*, 2009; *Gu and Sacchi*, 2009]; i.e., upper mantle heterogeneities that strongly influence the common S ray segment of *P410s* and *P660s* beneath stations likely persist after the tomographic model–based travel time corrections. This scenario is not unexpected considering the combination of two related factors, 1) the difficulty of making an accurate assessment of amplitude information using ray theoretical kernels [*Li and Romanowicz*, 1996; *Liu and Gu*,

2012; *Zhou et al.*, 2004], especially in view of a steep gradient in temperature and composition between the core of Precambrian cratons and the much younger terranes, and 2) severe smoothing during tomographic inversions for regions such as Alberta, where data coverage is problematic.

4.4.2 Structures Above 400 km

Corroborating evidence is provided by the regional variation of discontinuity depths for stations residing in the south–west of the study region, particularly those along the Rocky Mountain foreland belt (e.g., BRU, NOR, WALA, SLEB, CLA). The average depths measured at this cluster of stations are ∼424.6 km and 675.6 km, respectively, for the *410* and *660*; these are 14 km & 13.6 km greater than the remaining stations, on average. This regional topographic pattern is well correlated with the predicted seismic velocity variations in the lithospheric mantle, where the contrast between the low velocity terranes of the Rockies and the high velocity Archean/Palaeoproterozoic interior is among the sharpest such transitions found globally [*Nettles and Dziewonski*, 2008]. This prominent north–east to south–west transition has been well documented through global [*Grand*, 1994; *Grand et al.*, 1997] and regionally focused [*Frederiksen et al.*, 2001; *Mercier et al.*, 2009; *Nettles and Dziewonski*, 2008; *van der Lee and Nolet*, 1997] tomographic inversions, and the velocity gradient may persist down to depths of ∼400 km [*Mercier et al.*, 2009]. Based on our receiver function analysis, the excess topography of the MTZ discontinuities could imply even greater influences by the Moho depth and/or upper mantle heterogeneities. Corrections due to crustal thickness variations are generally positive, which has the equivalent effect of elevating the MTZ interfaces (Figure 4.5). Such effects could be more significant than previously depicted according to updated crustal models of *Gu et al.* [2011, 2012] using an improved regional seismic database.

Still, the difference in the model corrections is no more than 0.367 s (0.136 s on average), which amounts to 1.25–3.25 km in at discontinuity depths and falls short of explaining the regional depths of the MTZ discontinuities.

The effect of the heterogeneity correction for the top 400 km of the mantle is positive, which counteracts the influence of the crustal corrections, due to the higher–than–average velocities in the upper mantle portion of ND2008 in this region. As seen in Figure 4.12, increasing both the P and S velocities results in a reduced differential time relative to PREM. The total correction (sum of the crustal and mantle corrections) needs to be more negative in order to reconcile the discrepancy in delay times and explain the overall depression of the MTZ discontinuities. The necessary adjustment to the mantle correction may be accomplished through either the reduction of the absolute velocities (while maintaining a constant V_p/V_s ratio) or by increasing the V_p/V_s ratio used to scaled the shear velocity profile. Either one alone or a combination of these treatments would increase the differential time through the mantle model relative to PREM, and thus lower the correction (defined as $T_{PREM} - T_{modelled}$), and reduce the Pds–P delay time, thereby reducing the measured depth to the conversion interface. The combination of velocity reduction and V_p/V_s ratio increase would likely require diffuse partial melt or increased water content in the mantle above 410 km [*van der Lee and Nolet*, 1997]. The observed arrival time of the *P410s* measurement from the regional Radon panel is 44.7 seconds, which is 1.03 s slower than the PREM–predicted arrival time of 43.67s and amounts to a difference of 2.3%.

In order to quantify the velocity perturbation sufficient to explain the observed anomalous delay times, we compute vertical incidence delay times with PREM shear velocity as the background model, for two 'styles' of velocity perturbation. We first compute the theoretical delay time anomaly by increasing both P and S velocities

while keeping their ratio constant, and then perform a similar experiment by fixing the shear wave velocity while varying the V_p. The resulting curves show opposite slopes, with the delay time growing proportionally to the V_p/V_s ratio and decreasing with an increase in absolute velocity. To assess the relative strength of these two approaches, we plot the V_p/V_s curve in reverse and the resulting positive delays show comparable amplitudes and trends to those resulting from a constant ratio; the effect of the scaled V_p/V_s ratio becomes slightly more pronounced as delay time decreases. This sensitivity test (Figure 4.12) suggests the probable cause(s) of the residual MTZ discontinuity topography as 1) a $\sim$2.5% decrease in both V_p and V_s, 2) an increase in the V_s/V_s ratio of $\sim$2%, or 3) a combination of the two. All three candidates would imply a sharper transition between cratons and terranes, and the requisite velocities may be accommodated by pockets of partial melt or volatiles in the upper mantle. A hydrated upper mantle, in connection with the nearby Cascadia subduction along the Pacific west coast or the Mesozoic–era subduction of the Kula and Farallon plates, offers a viable explanation.

Alternatively, the required thermal and/or compositional variation responsible for the excess discontinuity topography may be confined to a localized anomaly. For instance, a global thin low velocity layer atop the *410* [*Bercovici and ichiro Karato*, 2003; *Tauzin et al.*, 2010] has the equivalent effect of a distributed melt fraction in depressing both discontinuities. A hydrous layer atop the *410* has been identified in East Asia [*Huang and Zhao*, 2006], which could provide the source of partial melting for the Changbai and Wu Da Lian Chi hotspots [*Zhao*, 2001]. A similar layer has also been suggested to reside within the Tonga slab [*Zheng et al.*, 2007] and to the east of the Nazca–South America subduction zone [*Contenti et al.*, 2012; *Schmerr and Garnero*, 2007]. However, while a low velocity structure was modeled by *Schaeffer and Bostock* [2010] within the Cordillera, its existence has not been
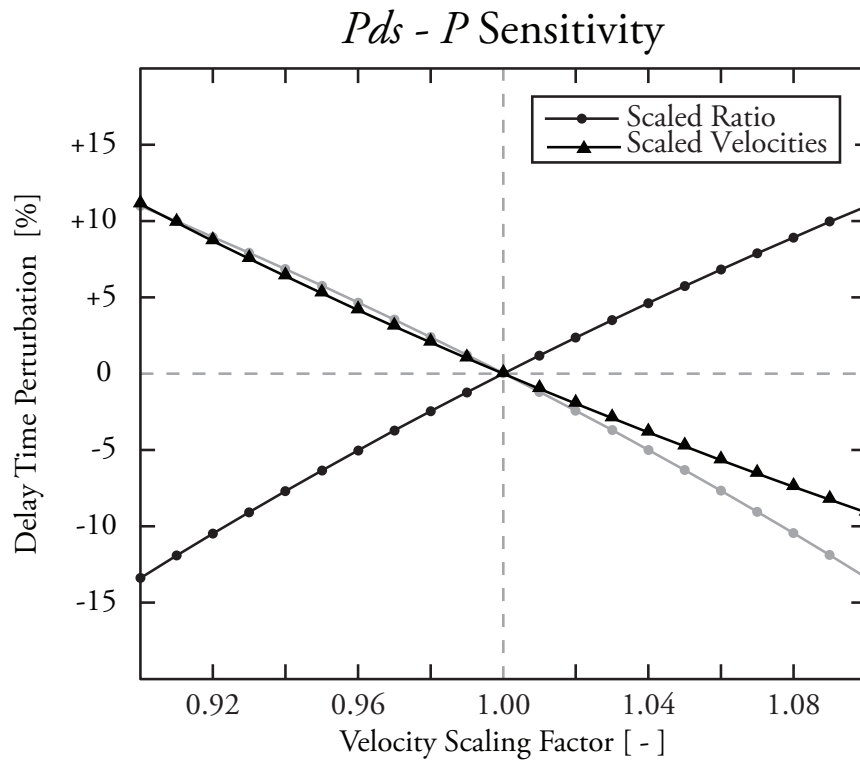
Figure 4.12: Sensitivity analysis for upper mantle anomalies. Filled black circles show the result of scaling both V_p and V_s, while maintaining a constant V_p/V_s ratio. Filled triangles shows the result of scaling the V_p/V_s ratio. The grey line shows a flipped version of the constant–ratio test, in order to show the relative trend of the two curves.

well established in the asthenosphere below the craton-terrane boundary zone.

4.4.3   MTZ Thickness and Interpretations

Unlike the absolute depths of the *410* and *660*, which are strongly affected by the structure above the MTZ, the difference between *P660s* and *P410s* delay times (or MTZ thickness) is primarily sensitive to the seismic velocities within the MTZ. As indicated in Section 4.4.1, previous studies that include data from this region have generally inferred gradual thickening of the MTZ from the Cordillera [*Bostock*, 1996; *Tauzin et al.*, 2008] to an average value beneath the core of the North American craton. Our results indicate that such an west–to–east transition may not be as monotonic or smooth as suggested by these global studies (Figure 4.10c). The average MTZ thickness (243 km) from the northern stations (EDM, PER, BRU, NOR, and CZA) is comparable to the averages of 246 km and 247 km obtained in previous global *Pds* studies [*Lawrence and Shearer*, 2006; *Tauzin et al.*, 2008] as well as to the average MTZ thickness of 242 km obtained via global *SS* precursor analysis [*Flanagan and Shearer*, 1998; *Gu and Dziewoński*, 2002]. However, the four southern stations (WALA, LYA, SLEB, CLA) posted an average thickness of 258 km, which exceeds the 2σ uncertainty estimate of the northern stations. The average thickness is dominated by the measurement at LYA of 266 km, but the average thickness remains significant (255 km) without LYA. The MTZ thickness in the southern portion of the CRANE array is comparable to the global subduction zone average of 263 km [*Tauzin et al.*, 2008], as well as to estimates from regional studies of subduction zones in eastern China (256 km, *Gao et al.* [2010]; 258 km, *Shen et al.* [2008], Japan ($\sim$255 km, *Li et al.* [2000], up to 280 km, *Niu et al.* [2005]), South America (270 km, *Liu et al.* [2003]) and the Mediterranean ($\sim$252 km, *van der Meijde et al.* [2005]).

MTZ thickening relative to *SS* precursor results has been previously documented in studies of *Pds* phases [*Lawrence and Shearer*, 2006; *Tauzin et al.*, 2008], and is generally attributed to the preferential sampling of continental, rather than oceanic, mantle by the receiver functions. In our study region, the velocity pattern of ND2008 is generally consistent with that of the MTZ thickness variations, with decreasing corrections in southern Alberta. However, the extent of the north–south MTZ thickening is considerably under–predicted by the velocity model. The excess *660* depression over *410* and residual MTZ thickness after corrections are evidence of a high velocity zone near the base of the MTZ. In view of the Mesozoic tectonic history of North America, the thermal anomaly could be caused by a remnant of the subducted Farallon/Kula plates. In fact, recent studies have revealed a subducted Farallon slab residual thermal anomaly of up to 400℃[*Schmid et al.*, 2002]. This value is closer to thermal equilibrium than an actively subducting slab but remains capable of causing upwards of 19 km of depression of the *660* based on an experimentally determined Clapyeron slope of -2.0 MPa/K°[*Helffrich*, 2000]. In other words, the equivalent thermal anomaly from seismic tomography is well within the range exhibited by the average MTZ thickness perturbation of 15 km from three southern stations and a maximum perturbation of 23 km at station LYA. Our observations are also in excellent correlation with the proposed velocity structure of the North American mantle (Figure 4.13) based on recent tomographic inversions e.g., *Simmons et al.* [2010]. The high velocity anomaly near the south–western corner of Alberta, which extends southward into the United States [*Simmons et al.*, 2010], and the corroborating evidence of a thick MTZ (this study) make a compelling argument for the presence of a small, abandoned, and unequilibrated slab fragment in the MTZ.

The effect of such a small–scale feature may be averaged out in global *SS* precursor studies, due to the Fresnel zone of the phases used, and the large cap size
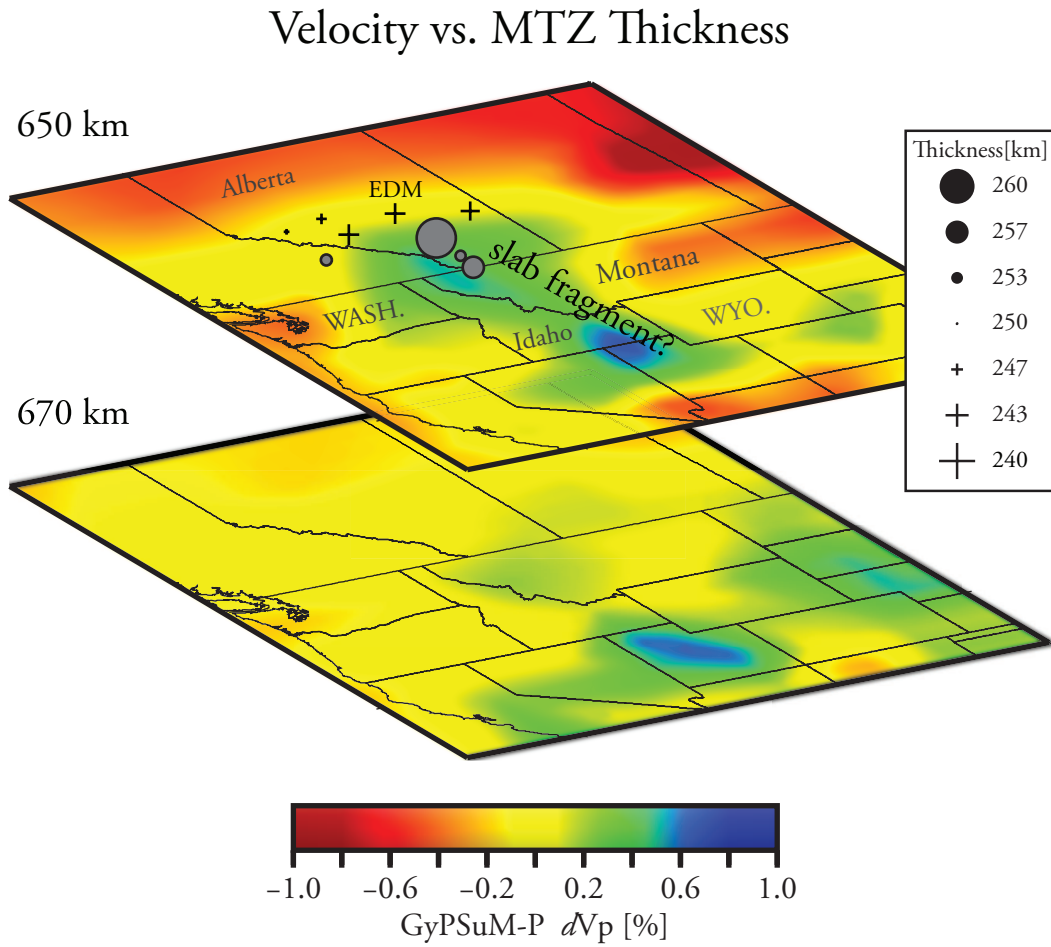
Figure 4.13: Slices at 600 km, 625 km, 650 km, and 670 depth through a portion of the GyPSuM *P* velocity model of *Simmons et al.* [2010] showing a localized high velocity anomaly (green and blue colors) in southern Alberta, Idaho, and Montana. MTZ thickness values are overlain on the 650 km slice.

typically employed for noise attenuation. Thus, the lateral extent of possible MTZ thickening beneath the Cordillera remains uncertain due to the sparsity of station coverage surrounding our array, although if our interpretation is correct, the extent of MTZ thickening should remain limited to region within the cold anomaly present in the GyPSuM model. This issue will be partially resolved in the near future, as the large-scale analysis of the USArray data is likely to involve a significant effort to compute and interpret receiver functions across the continental United States.

4.5 Conclusions

By analyzing 5+ years of continuous recordings from CRANE and CNSN stations, we have been able to reliably determine the mantle reflectivity structures beneath the craton–terrane boundary in western Canada. While both station density and the data volume of existing stations benefit from the ongoing efforts in the study region [*Gu et al.*, 2011], the outcomes of this study shed new light on the behaviours, and hence the associated thermal and compositional variations, of the two major MTZ phase boundaries. The key observations and their implications for the mantle structure and dynamics are summarized as follows:

1. Both the 410 and 660 km seismic discontinuities are strongly depressed in the Alberta Basin and eastern Cordillera, especially in the latter region, suggesting strong influence from heterogeneities in the mantle above the MTZ.

2. The southwestward dipping MTZ phase boundaries correlate with the pattern of mantle heterogeneities in the top 400 km, which suggests a strong thermal gradient across the craton (east) to terrane (west) transition. Diffuse or localized compositional variations (e.g., partial melt) may also be present in view of the large magnitude of the average depressions.

3. The MTZ thickens toward the southernmost Alberta. The north–south disparity in thickness, which is sufficiently explained by the existing models of MTZ seismic velocities, could be evidence of an unequilibrated remnant of the subducted Farallon–Kula plate near the base of the MTZ in southern Alberta and north–western US.

In short, the absolute and differential depths of the two major MTZ phase boundaries appear to be strong functions of mantle temperature beneath the western boundary of the North American craton. A sharp mantle gradient is expected in the upper 300–400 km of the mantle, where a thermally unequiblibrated Mesozoic slab fragment may persist within the MTZ. These inferences may provide further insights on the formation and modification of western Canada.

CHAPTER 5

Conclusions

As previously discussed, the *SS* precursor method employed in Chapter 3 provides a valuable tool for interrogating mantle structure both on a global scale and in regions that may be under–sampled by higher–resolution methods. The resolution of these phases renders them primarily useful for the global mapping of transition zone discontinuities. The method may also be useful for regional studies, where bounce–point density is sufficiently high; however, they are limited by both the large Fresnel zone of the phase and the typical filters used in processing as to the small–scale variability that may be reliably detected. Furthermore, a recent study has used synthetic seismograms computed through fully three–dimensional velocity models [*Komatitsch et al.*, 2004; *Tromp et al.*, 2008] to demonstrate that some effects, such as a doubled precursor peak at 660 km depth, may indicate the presence of strong station–side heterogeneity, rather than the existence of multiple layers near the ray–path mid–point [*Zheng and Romanowicz*, 2012]. Despite these potential issues, the *SS* precursor method remains a valuable tool in the investigation of sharp mantle structure, due to the global coverage of *SS* bounce–points and the volume of

data available for analysis.

The receiver function method discussed in Chapter 4 involves the deconvolution of the vertical from the radial shear component seismogram in order to isolate the arrivals of P–S converted waves beneath the recording stations. This high–resolution method provides good constraint on the local variability of the MTZ in regions where station density is high. These two methods are highly complementary. The geometry of the SS precursor allows for investigation in station–poor regions where the receiver function approach is limited, and the high depth resolution and increased sensitivity to local variability and azimuthal effects allows the receiver function method to provide valuable constraint on the results obtained by global reflected–phase studies. The use of these two methodologies allows the construction of a more complete picture than is provided by either approach alone.

Beyond the complementary nature of the two methods utilized in this thesis, the areas studied also have some overlap in terms of general tectonics and regional history. Both study areas involve a long history of convergence of oceanic plates with continental plates: the Nazca slab subducting beneath South America since the late Cretaceous [*Bird*, 2003; *Pardo-Casas and Molnar*, 1987; *Russo and Silver*, 1996], and the Juan de Fuca plate subducting beneath North America along the Cascadia subduction zone for at least 200 My [*Monger and Price*, 2002]. However, the similarity between the two regions should not be overstated. The previous subduction of the Farallon slab resulted in the accretion of the belts of the Canadian Cordillera, which produces a lateral separation of ~800 – 900 km between the surface expression of the Juan de Fuca subduction and the margin of the North American craton. This is a far greater trench–craton distance than in South America, where the width of the Andean Cordillera averages 200 – 400 km. This may have implications for the transition between oceanic and cratonic influences on the upper mantle and

transition zone discontinuities.

The results obtained in the analysis of the mantle beneath South and North America generally agree with previous research. The variability of the *660* near the Nazca slab, interpreted as evidence of partial slab stagnation and internal buckling, is similar to observations of deformation of the *660* in the presence of stagnant slab material beneath northern Japan [*Gu et al.*, 2012]. In northern Honshu, seismic tomography indicates that the downwelling slab is mostly stagnant, whereas similar studies in South America show a significant fast anomaly in the lower mantle, evidence for slab continuation beneath the MTZ [*Montelli et al.*, 2004]. In light of this, we have interpreted the variability of the *660* in South America to be caused by slab buckling and deformation facilitated by the high convergence rate of the Nazca and South American plates. However, this ponding appears to be temporary, with slab material continuing into the lower mantle. The observed variability of the *660* is overlain by a broad "reflection gap" on the *410*, which we interpret as evidence of a compositional anomaly atop the MTZ. Studies in northern China [*Revenaugh and Sipkin*, 1992] and previous studies of South America [*Schmerr and Garnero*, 2007] support the concept of the *410* as a "water filter", with the dehydration of subducting material creating a hydrated lens atop the discontinuity. Studies of north-western North America have also observed evidence of a low–velocity layer in the mantle above the *410* [*Schaeffer and Bostock*, 2010]. Work done to image the MTZ beneath the far interior of the North American continent, also using receiver functions, has indicated a simple transition zone [*Thompson et al.*, 2011] with relatively little perturbation of the *410* and *660*; this is consistent with the relatively uniform MTZ thickness across the northern portion of the CRANE array. The thick MTZ located at the southern corner of the array, interpreted as a fragment of subducted slab, is consistent with a localized high–velocity anomaly present in the GyPSuM mantle velocity/density

model [*Simmons et al.*, 2010], though the lateral extent of the thickening is not well constrained to the south due to the limited footprint of the CRANE array.

Future work to more accurately resolve mantle structure may take many forms. Methods similar to SS precursors, using higher frequency phases such as PP and $P'P'$, may provide a link between the resolutions of the SS and receiver function methods, allowing for the analysis of structure across a continuous frequency band. High quality data sampling the same region at varying resolutions may provide insight into the depth range of occurence of the phase transitions that give rise to the *410* and *660*, as well as providing more complete maps of these interfaces. These phases could potentially be combined with body and surface wave travel–time measurements into a joint tomographic/topographic inversion that simultaneously trade–off smooth mantle velocity variations and sharp boundary depth variability, such as was performed by [*Gu et al.*, 2003]. The addition of adjoint tomography (see *Liu and Gu* [2012] and references therein) to this problem may further increase the reliability and stability of the resulting models, as well as ensuring that the inverted model satisfactorily reproduces the data input. Research currently being done on the application of more sophisticated signal processing techniques to long–distance reflected phases– for example, the deconvolution of the SS wavelet from the precursor time window –has the potential to improve the depth resolution of the phases, and the application of Radon inversion [*Schultz and Gu*, 2012] to the results may allow for the discrimination of true underside reflections from the perhaps spurious arrivals due to station–side structure as posited by *Zheng and Romanowicz* [2012]. The continued accumulation of data at the CRANE array, particularly at azimuths where earthquakes are more infrequent, may allow for investigation into the anisotropic structure of the Western Canadian lithosphere and may assist in the interpretation of shear wave (SKS) splitting results [*Currie et al.*, 2004; *Gu et al.*, 2011], where

azimuthal variations in the shear–wave splitting parameters have indicated significant complexity in the crust and mantle beneath the craton. Lastly, crustal modelling using the CRANE data has the potential to ameliorate one of the major sources of uncertainty in the interpretation of MTZ *P–s* conversion, the effect of crustal characteristics on observed delay times. Improved crustal thickness and velocity values may would improve the corrections applied to the MTZ results, as well as providing insight into the processes that involved in forming the craton and the subsequent collisions that expanded North America to its present day configuration.

Bibliography

Agee, C. B., Phase transformations and seismic structure in the upper mantle and transition zone, *Reviews in Mineralogy and Geochemistry*, *37*(1), 165–203, 1998.

Akaogi, M., H. Takayama, H. Kojitani, H. Kawaji, and T. Atake, Low temperature heat capacities, entropies and enthalpies of Mg_2SiO_4 polymorphs, and $\alpha - \beta - \gamma$ and post–spinel phase relations at high pressure, *Phys. Chem. Miner.*, *34*, 169–183, 2007.

Ammon, C. J., The isolation of receiver effects from teleseismic p waveforms, *Bulletin of the Seismological Society of America*, *81*(6), 2504–2510, 1991.

An, Y., Y. J. Gu, and M. D. Sacchi, Imaging mantle discontinuities using least squares radon transform, *J. Geophys. Res.*, *112*, doi:10.1029/2007JB005009, 2007.

Barazangi, M., and B. L. Isacks, Spatial distribution of earthquakes and subduction of the Nazca plate beneath South America, *Geology*, *4*, 686–692, 1976.

Bassin, C., and G. Laske, The current limits of resolution for surface wave tomography in North America, *Eos. Trans. AGU*, *81*, fall Meet. Suppl. F897, 2000.

Ben-Menaham, A., A concise history of mainstream seismology: origins, legacy, and perspectives, *Bull. Seis. Soc. Am.*, *85*(4), 1202–1225, 1995.

Bercovici, D., and S. ichiro Karato, Whole-mantle convection and the transition-zone water filter, *Nature*, *425*, 39–44, doi:10.1038/nature01918, 2003.

Bevis, M., E. C. Kendrick, R. S. Jr., T. Herring, J. Godoy, and F. Galban, Crustal motion north and south of the Arica deflection: Comparing recent geodetic results from the central Andes, *Geochem. Geophys. Geosyst.*, *1*(12), 1–10, 1999.

Bevis, M., E. Kendrick, R. S. Jr., B. Brooks, R. Allmendinger, and B. Isacks, On the strength of interplate coupling and the rate of back arc convergence in the central Andes: An analysis of the interseismic velocity field, *Geochem. Geophys. Geosyst.*, *2*(11), 2001.

Beylkin, G., Discrete Radon transform, *IEEE Trans. Acoust., Speech and Signal Proc.*, *ASSP-35*, 1987.

Bijwaard, H., W. Spakman, and E. R. Engdahl, Closing the gap between regional and global travel time tomography, *J. Geophys. Res.*, *103*(B12), 30,055–30,078, 1998.

Bijward, H., W. Spakman, and E. R. Engdahl, Closing the gap between regional and global travel time tomography, *J. Geophys. Res.*, *103*(B12), 30,055–30,078, 1998.

Bina, C. R., Seismological constraints upon mantle composition, *Treatise on Geochemistry*, *2*, 39–59, 2003.

Bina, C. R., and G. Helffrich, Phase transition Clapeyron slopes and transition zone seismic discontinuity topography, *J. Geophys. Res.*, *99*(B8), 15,853–15,860, doi:10.1029/94JB00462, 1994.

Bird, P., An updated digital model of plate boundaries, *Geochem. Geophys. Geosyst.*, *4*(3), 1027, doi:10.1029/2001GC000252, 2003.

Blum, J., and Y. Shen, Thermal, hydrous, and mechanical states of the mantle transition zone beneath southern africa, *Earth and Planetary Science Letters*, *217*(34), 367 – 378, doi:10.1016/S0012-821X(03)00628-9, 2004.

Bostock, M. G., A seismic image of the upper mantle beneath the north american craton, *Geophys. Res. Lett.*, *23*(13), doi:10.1029/96GL00972, 1996.

Bostock, M. G., D. W. Eaton, and D. B. Snyder, Teleseismic studies of the canadian landmass: Lithoprobe and its legacy, *Can. J. Earth Sci.*, *47*, 2010.

Bullen, K. E., Seismology and the earth's deep interior, *Aust. J. Sci.*, *19*, 99–100, 1956.

Bunge, H.-P., and S. Grand, Mesozoic plate-motion history below the northeast Pacific Ocean from seismic images of the subducted Farallon slab, *Nature*, *405*, 337 – 340, 2000.

Cadzow, J. A., Signal enhancement – a composite property mapping algorithm, *IEEE Trans. Acous. Speech Sign. Proc.*, *36*(1), 1988.

Cahill, T., and B. L. Isacks, Seismicity and shape of the subducted Nazca Plate, *J. Geophys. Res.*, *97*(B12), 17,503–17,529, 1992.

Candes, E. J., and B. Recht, Exact matrix completion via convex optimization, *Foundations of Computational Mathematics*, *9*(6), doi:10.1007/s10208-009-9045-5, 2009.

Cassidy, J. F., Numerical experiments in broadband receiver function analysis, *Bull. Seis. Soc. Am.*, *82*(3), 1453–1474, 1992.

Cassidy, J. F., A comparison of the receiver structure beneath stations of the

canadian national seismograph network, *Canadian Journal of Earth Sciences*, *32*(7), 938–951, doi:10.1139/e95-079, 1995.

Chaljub, E., and A. Tarantola, Sensitivity of SS precursors to topography on the upper-mantle 660-km discontinuity, *Geophys. Res. Lett.*, *24*(21), 2613–2616, 1997.

Chambers, K., J. H. Woodhouse, and A. Deuss, Topography of the 410-km discontinuity from PP and SS precursors, *Earth Planet. Sci. Lett.*, *235*, 610–622, 2005.

Chevrot, S., L. Vinnik, and J.-P. Montagner, Global scale analysis of the mantle *Pds* phases, *J. Geophys. Res.*, *104*(B9), 20,203–20,219, 1999.

Clarke, T. J., P. G. Silver, Y. Yeh, D. E. James, T. C. Wallace, and S. L. Beck, Close in ScS and sScS reverberations from the 9 June 1994 Bolivian earthquake, *Geophys. Res. Lett.*, *22*(16), 2313–2316, doi:10.1029/95GL02062, 1995.

Clowes, R. M., M. J. A. Burianyk, A. R. Gorman, and E. R. Kanasewich, Crustal velocity structure from SAREX, the Southern Alberta Refraction Experiment, *Can. J. Earth Sci.*, *39*, doi:10.1139/E01-070, 2002.

Contenti, S. M., Y. J. Gu, A. Okeler, and M. D. Sacchi, Shear wave reflectivity imaging of the nazca-south america subduction zone: stagnant slab in the mantle transition zone?, *Geophys. Res. Lett.*, *39*(L02310), doi:10.1029/2011GL050064, 2012.

Courtier, A. M., and J. Revenaugh, A water-rich transition zone beneath the eastern United States and Gulf of Mexico, in *Earth's Deep Water Cycle*, edited by S. Jacobsen and S. van der Lee, AGU Monograph, 2006.

Courtier, A. M., J. Revenaugh, M. G. Bostock, J. B. Gaherty, and E. J. Garnero,

Upper mantle discontinuity structure from receiver functions along the CANOE array, in *AGU Fall Meeting 2006*, AGU, 2006.

Crotwell, H. P., and T. J. Owens, Automated receiver function processing, *Seismol. Res. Lett.*, *76*(6), 2005.

Crotwell, H. P., J. Owens, and J. Ritsema, The TauP toolkit: Flexible seismic travel-time and ray-path utilities, *Seismo. Ret. Lett.*, *70*, 154–160, 1999.

Currie, C. A., and R. D. Hyndman, The thermal structure of subduction zone back arcs, *J. Geophys. Res.*, *111*(B08404), doi:10.1029/2005JB004024, 2006.

Currie, C. A., J. F. Cassidy, R. D. Hyndman, and M. G. Bostock, Shear wave anisotropy beneath the Cascadia subduction zone and western North American craton, *Geophys. J. Int.*, *157*, 341–353, doi:10.1111/j.1365-246X.2004.02175.x, 2004.

Dalton, C. A., J. B. Gaherty, and A. M. Courtier, Crustal v_s structure in northwestern Canada: Imaging the Cordillera-craton transition with ambient noise tomography, *J. Geophys. Res.*, *116*(B12315), doi:10.1029/2011JB008499, 2011.

Data Announcement 88-MGG-02, *Digital relief of the Surface of the Earth*, NOAA, National Geophysical Data Center, Boulder, Colorado, U.S.A., 1998.

Deon, F., M. Koch-Mller, D. Rhede, and R. Wirth, Water and iron effect on the p-t-x coordinates of the 410-km discontinuity in the earth upper mantle, *Contributions to Mineralogy and Petrology*, *161*, 653–666, doi:10.1007/s00410-010-0555-6, 2011.

Deuss, A., Global observations of mantle discontinuities using ss and pp precursors, *Surveys in Geophysics*, *30*, 301–326, 10.1007/s10712-009-9078-y, 2009.

Deuss, A., and J. H. Woodhouse, A systematic search for mantle discontinuities using SS-precursors, *Geophys. Res. Lett.*, *29*(8), 1249, doi:/10.1029/2002GL014768, 2002.

Dziewoński, A. M., and D. L. Anderson, Preliminary reference earth model, *Phys. Earth Planet. Int.*, *25*(4), 297–356, doi:10.1016/0031-9201(81)90046-7, 1981.

Eaton, D. W., and J. F. Cassidy, A relic Proterozoic subduction zone in western Canada: New evidence from seismic reflection and receiver function data, *Geophys. Res. Lett.*, *23*(25), 1996.

Efron, B., and R. Tibshirani, Statistical data analysis in the computer age, *Science*, *253*(5018), 390–395, doi:10.1126/science.253.5018.390, 1991.

Engdahl, E. R., R. D. van der Hilst, and J. Berrocal, Imaging of subducted lithosphere beneath South America, *Geophys. Res. Lett.*, *22*(16), 1995.

Fei, Y., et al., Experimentally determined postspinel transformation boundary in Mg_2SiO_4 using mgo as an internal pressure standard and its geophysical implications, *J. Geophys. Res.*, *109*(B02305), doi:10.1029/2003JB002562, 2004.

Flanagan, M. P., and P. M. Shearer, Global mapping of topography on transition zone velocity discontinuities by stacking SS precursors, *J. Geophys. Res.*, *103*(B2), 2673–2692, 1998.

Frederiksen, A. W., M. G. Bostock, and J. F. Cassidy, S-wave velocity structure of the Canadian upper mantle, *Phys. Earth. Planet. Int.*, *124*, 2001.

Fuchs, K., and G. M. Müller, Computation of synthetic seismograms with the reflectivity method and comparisons with observations, *Geophys. J. R. astr. Soc.*, *23*, 417–433, 1971.

Fukao, Y., S. Widiyantoro, and M. Obayashi, Stagnant slabs in the upper and lower mantle transition region, *Rev. Geophys.*, *39*(3), 291–323, 2001.

Fukao, Y., M. Obayashi, T. Makakuki, and the Deep Slab Project Group, Stagnant slab: A review, *Annu. Rev. Earth. Planet. Sci.*, *37*, 19–46, 2009.

Gao, Y., D. Suetsugu, Y. Fukao, M. Obayashi, Y. Shi, and R. Liu, Seismic discontinuities in the mantle transition zone and at the top of the lower mantle beneath eastern China and Korea: Influence of the stagnant Pacific slab, *Phys. Earth Planet. Int.*, *183*, 288–295, 2010.

Gorman, A. R., et al., Deep Probe: imaging the roots of western North America, *Can. J. Earth Sci.*, *39*, doi:10.1139/E01-064, 2002.

Grand, S. P., Mantle shear structure beneath the Americas and surrounding oceans, *J. Geophys. Res.*, *99*(B6), 11,591–11,621, doi:10.1029/94JB00042, 1994.

Grand, S. P., Mantle shear–wave tomography and the fate of subducted slabs, *Philosophical Transactions of the Royal Society of London. Series A: Mathematical, Physical and Engineering Sciences*, *360*(1800), 2475–2491, 2002.

Grand, S. P., and D. V. Helmberger, Upper mantle shear structure of north america, *Geophysical Journal of the Royal Astronomical Society*, *76*(2), 399–438, doi:10.1111/j.1365-246X.1984.tb05053.x, 1984.

Grand, S. P., R. D. van der Hilst, and S. Widiyantoro, Global seismic tomography: A snapshot of convection in the earth,, *GSA Today*, *7*(4), 1997.

Gu, Y., A. M. Dziewoński, and C. B. Agee, Global de-correlation of the topography of transition zone discontinuities, *Earth Planet. Sci. Lett.*, *157*(1-2), 57–67, doi:10.1016/S0012-821X(98)00027-2, 1998.

Gu, Y. J., and A. M. Dziewoński, Global variability of transition zone thickness, *J. Geophys. Res.*, *107*(B7), 2135, doi:/10.1029/2001JB000489, 2002.

Gu, Y. J., and M. D. Sacchi, Radon transform methods and their applications in mapping mantle reflectivity structure, *Surv. Geophys*, doi:10.1111/j.1365-246X. 2009.04042.x, 2009.

Gu, Y. J., A. M. Dziewoński, and G. Ekström, Simultaneous inversion for mantle shear velocity and topography of transition zone discontinuities, *Geophys. J. Int.*, *154*, 559–583, 2003.

Gu, Y. J., A. Okeler, L. Shen, and S. Contenti, The Canadian Rockies and Alberta Network (CRANE): New Constraints on the Rockies and Western Canada Sedimentary Basin, *Seismo. Res. Lett.*, *82*(4), doi:10.1785/gssrl.82.4.575, 2011.

Gu, Y. J., A. Okeler, and R. Schultz, Tracking slabs beneath northwestern Pacific subduction zones, *Earth Planet. Sci. Lett.*, doi:10.1016/j.epsl.2012.03.023, 2012.

Gudmundsson, O., and M. Sambridge, A regionalized upper mantle (RUM) seismic model, *J. Geophys. Res.*, *103*(B4), 7121–7136, doi:10.1029/97JB02488, 1998.

Harms, T. A., and C. A. Evenchick, *Whence the Mountains? Inquiries into the Evolution of Orogenic Systems: A Volume in Honor of Raymond A. Price*, Geol. Sci. Am., 2007.

Heit, B., F. Sodoudi, X. Yuan, M. Bianchi, and R. Kind, An S receiver function analysis of the lithospheric structure in South America, *Geophys. Res. Lett.*, *34*(14), L14,307, doi:/10.1029/2007GL030317, 2007.

Helffrich, G., Topography of the transition zone seismic discontinuities, *Rev. Geophys.*, *38*, 141–158, 2000.

Herrmann, R. B., and C. Y. Wang, A comparison of synthetic seismograms, *Bull. Seism. Soc. Am.*, *75*, 41–56, 1985.

Hier-Majumder, S., and A. Courtier, Seismic signature of small melt fraction atop the transition zone, *Earth Planet. Sci. Lett.*, *308*(3-4), 334 – 342, doi:10.1016/j. epsl.2011.05.055, 2011.

Hoffman, P. F., United Plates of America, The Birth of a Craton: Early Proterozoic Assembly and Growth of Laurentia, *Annu. Rev. Earth Planet. Sci.*, *16*, 543–603, doi:10.1146/annurev.earth.16.1.543, 1988.

Houser, C., and Q. William, Reconciling Pacific 410 and 660 km discontinuity topography, transition zone shear velocity patterns, and mantle phase transitions, *Earth. Planet. Sci. Lett.*, doi:10.1016/j.epsl.2010.05.006, 2010.

Houser, C., G. Masters, M. Flanagan, and P. Shearer, Determination and analysis of long-wavelength transition zone structure using SS precursors, *Geophys. J. Int.*, *174*(1), 178–194, doi:10.1111/j.1365-246X.2008.03719.x, 2008.

Huang, J., and D. Zhao, High-resolution mantle tomography of china and surrounding regions, *J. Geophys. Res.*, *111*(B09305), doi:10.1029/2005JB004066, 2006.

Irifune, T., et al., The postspinel phase boundary in Mg_2SiO_4 determined by in situ X-ray diffraction, *Science*, *279*, 1698–1700, doi:10.1126/science.279.5357.1698, 1998.

Ita, J., and L. Stixrude, Petrology, elasticity, and composition of the mantle transition zone, *J. Geophys. Res.*, *97*(B5), 6849–6866, doi:10.1029/92JB00068, 1992.

James, D. E., and J. A. Snoke, Seismic Evidence for Continuity of the Deep Slab Beneath Central and Eastern Peru, *J. Geophys. Res.*, *95*(B4), 4989–5001, 1990.

Katsura, T., and E. Ito, The system Mg2SiO4-Fe2SiO4 at high pressures and temperatures: Precise determination of stabilities of olivine, modified spinel, and spinel, *J. Geophys. Res.*, *94* (B11), 15,663–15,670, doi:198910.1029/JB094iB11p15663, 1989.

Katsura, T., et al., Post-spinel transition in Mg_2SiO_4 determined by high P-T in situ X-ray diffractometry, *Phys. Earth. Planet. Inter.*, *136*, 11–24, doi:10.1016/S0031-9201(03)00019-0, 2003.

Katsura, T., et al., Olivine-wadsleyite transition in the system $(Mg,Fe)_2SiO_4$, *J. Geophys. Res.*, *109* (B02209), doi:10.1029/2003JB002438, 2004.

Kawakatsu, H., and F. Niu, Seismic evidence for a 920-km discontinuity in the mantle, *Nature*, *371* (6495), 301–305, doi:10.1038/371301a0, 1994.

Kennett, B. L. N., *Seismic Wave Propagation in Stratified Media*, Cambridge University Press, pp. 167, 1983.

Klotz, J., et al., GPS-derived deformation of the central Andes including the 1995 Antofagasta Mw = 8.0 earthquake, *Pure and Applied Geophysics*, *154* (3-4), 709–730, doi:10.1007/s000240050249, 1999.

Komatitsch, D., Q. Liu, J. Tromp, P. Suss, and C. Stidham, Simulations of ground motion in the Los Angeles basin based upon the spectral–element method, *Bull. Seism. Soc. Am.*, *94*, 187–206, 2004.

Kreemer, C., W. E. Holt, and A. J. Haines, An integrated global model of present-day plate motions and plate boundary deformation, *Geophys. J. Int.*, *154* (1), 8–34, doi:10.1046/j.1365-246X.2003.01917.x, 2003.

Lallemand, S., A. Heuret, C. Faccenna, and F. Funiciello, Subduction dynamics as revealed by trench migration, *Tectonics*, *27* (TC3014), doi:10.1029/2007TC002212, 2008.

Langston, C. A., Corvallis, oregon, crustal and upper mantle receiver structure from teleseismic p and s waves, *Bulletin of the Seismological Society of America*, *67*(3), 713–724, 1977.

Langston, C. A., Structure under mount rainier, washington, inferred from teleseismic body waves, *J. Geophys. Res.*, *84*(B9), 4749–4762, 1979.

Lawrence, J. F., and P. M. Shearer, A global study of transition zone thickness using receiver functions, *J. Geophys. Res.*, *111*, doi:10.1029/2005JB003973, 2006.

Lawrence, J. F., and P. M. Shearer, Imaging mantle transition zone thickness with SdS-SS finite-frequency sensitivity kernels, *Geophys. J. Int.*, *174*(1), 143–158, doi:10.1111/j.1365-246X.2007.03673.x, 2008.

Lehmann, I., P', *Bur. Ctr. seism. Int. A*, *14*, 3–31, 1936.

Levander, A., USArray design implications for wavefield imaging in the lithosphere and upper mantle, *The Leading Edge*, *22*(3), 250–255, doi:10.1190/1.1564530, 2003.

Li, C., R. D. van der Hilst, E. R. Engdahl, and S. Burdick, A new global model for P wave speed variations in Earth's mantle, *Geochem. Geophys. Geosyst.*, *9*(5), doi:10.1029/2007GC001806, 2008.

Li, X., S. V. Sobolev, R. Kind, X. Yuan, and C. Estabrook, A detailed receiver function image of the upper mantle discontinuities in the Japan subduction zone, *Earth Planet. Sci. Lett.*, *183*, 527–541, 2000.

Li, X. D., and B. Romanowicz, Global mantle shear velocity model developed using nonlinear asymptotic coupling theory, *J. Geophys. Res.*, *101*, 22,245–22,273, 1996.

Ligorria, J. P., and C. J. Ammon, Iterative deconvolution and receiver-function estimation, *Bull. Seism. Soc. Am.*, *89*(5), 1395–1400, 1999.

Liu, K. H., S. S. Gao, P. G. Silver, and Y. Zhang, Mantle layering across central South America, *J. Geophys. Res.*, *108*(B11), 2510, doi:10.1029/2002JB002208, 2003.

Liu, Q., and Y. Gu, Seismic imaging: From classical to adjoint tomography, *Tectonophysics*, doi:10.1016/j.tecto.2012.07.006, 2012.

Loiselet, C., J. Braun, L. Husson, C. L. C. de Veslud, C. Thieulot, P. Yamato, and D. Grujic, Subducting slabs: Jellyfishes in the Earth's mantle, *Geochem. Geophys. Geosyst.*, *11*(Q08016), doi:10.1029/1020GC003172, 2010.

Mercier, J. P., M. G. Bostock, P. Audet, J. B. Gaherty, E. J. Garnero, and J. Revenaugh, The teleseismic signature of fossil subduction: Northwestern Canada, *J. Geophys. Res.*, *113*(B4), 2008.

Mercier, J. P., M. G. Bostock, J. F. Cassidy, K. Dueker, J. B. Gaherty, E. J. Garnero, J. Revenaugh, and G. Zandt, Body-wave tomography of western canada, *Tectonophysics*, doi:10.1016/j.tecto.2009.05.030, 2009.

Mohorovicic, A., Das Beben vom 8 Okt 1909, *Jahrb. Meteorol. Obs. Zagreb.*, *9*, 1–63, 1909.

Monger, J. W. H., and R. A. Price, The canadian cordillera: Geology and tectonic evolution, *CSEG Rec. February 2002*, pp. 17 – 36, 2002.

Montelli, R., G. Nolet, F. A. Dahlen, G. Masters, E. R. Engdahl, and S. Hung, Finite-Frequency tomography reveals a variety of plumes in the mantle, *Science*, *303*(5656), 338–343, doi:10.1126/science.1092485, 2004.

Mooney, W. D., G. Laske, and G. Masters, CRUST5.1: A global crustal model at 5°x 5°, *J. Geophys. Res.*, *103*, 1998.

Neele, F., H. de Regt, and J. VanDecar, Gross errors in upper-mantle discontinuity topography from underside reflection data, *Geophys. J. Int.*, *129*, 194–204, 1997.

Nettles, M., and A. Dziewonski, Radially anisotropic shear velocity structure of the upper mantle globally and beneath North America, *J. Geophys. Res.*, *113*(B02303), doi:10.1029/2006JB004819, 2008.

Niu, F., A. Levander, S. Ham, and M. Obayashi, Mapping the subducting Pacific slab beneath southwest Japan with Hi-net receiver functions, *Earth Planet. Sci. Lett.*, *239*, 9–17, 2005.

Norabuena, E., L. Leffler-Griffin, A. Mao, T. Dixon, S. Stein, I. S. Sacks, L. Ocola, and M. Ellis, Space geodetic observations of Nazca-South America convergence across the central Andes, *Science*, *279*(5349), 358–362, 1998.

Obayashi, M., H. Sugioka, J. Yoshimitsu, and Y. Fukao, High temperature anomalies oceanward of subducting slabs at the 410-km discontinuity, *Earth Planet. Sci. Lett.*, *243*(1-2), 149–158, doi:10.1016/j.epsl.2005.12.032, 2006.

Ohtani, E., Water in the mantle, *ELEMENTS*, *1*(1), 25–30, 2005.

Olafsson, G., *The Radon transform, inverse problems, and tomography*, American Mathematical Society, 2006.

Oldham, R. D., Constitution of the interior of the earth as revealed by earthquakes, *Quart. J. Geol. Soc.*, *62*, 456–475, 1906.

Oropeza, V., The singular spectrum analysis method and its application to seismic data denoising and reconstruction, Ph.D. thesis, University of Alberta, 2010.

Oropeza, V., and M. D. Sacchi, Simultaneous seismic de-noising and reconstruction via Multichannel Singular Spectrum Analysis (MSSA), *Geophysics*, *76*(3), 2009.

Pardo-Casas, F., and P. Molnar, Relative motion of the Nazca (Farallon) and South American plates since Late Cretaceous time., *Tectonics*, *6*, 233, 1987.

Phillips, B. R., and N. Coltice, Temperature beneath continents as a function of continental cover and convective wavelength, *J. Geophys. Res.*, *115*(B04408), doi:10.1029/2009JB006600, 2010.

Quinteros, J., S. V. Sobolev, and A. A. Popov, Viscosity in transition zone and lower mantle: Implications for slab penetration, *Geophys. Res. Lett.*, *37*(L09307), doi:10.1029/2010GL043140, 2010.

Revenaugh, J., and S. A. Sipkin, Seismic evidence for silicate melt atop the 410-km mantle discontinuity, *Nature*, *369*, 1992.

Ribe, N., E. Stutsmann, Y. Ren, and R. van der Hilst, Buckling instabilities of subducted lithosphere beneath the transition zone, *Earth Planet. Sci. Lett.*, *254*, 172–179, doi:10.1016/j.epsl.2006.11.028, 2007.

Ringwood, A. E., *Composition and Petrology of the Earth's Mantle*, McGraw-Hill, New York, USA, 1975.

Ringwood, A. E., and T. Irifune, Nature of the 660-km seismic discontinuity: implications for mantle dynamics and differentiation, *Nature*, *331*, 1988.

Ritsema, J., H. J. van Heijst, and J. H. Woodhouse, Global transition zone tomography, *J. Geophys. Res.*, *109*(B2), B02,302, 2004.

Rondenay, S., Upper mantle imaging with array recordings of converted and scattered

teleseismic waves, *Surv. Geophys.*, *30*, 377–405, doi:10.1007/s10712-009-9071-5, 2009.

Ross, G. M., Evolution of Precambrian continental lithosphere in Western Canada: results from Lithoprobe studies in Alberta and beyond, *Can. J. Earth Sci.*, *39*, doi:10.1139/E02-012, 2002.

Ross, G. M., and D. W. Eaton, Proterozoic tectonic accretion and growth of western Laurentia: results from Lithoprobe studies in northern Alberta, *Can. J. Earth Sci.*, *39*, doi:10.1139/E01-081, 2002.

Ross, G. M., R. R. Parrish, M. E. Villeneuve, and S. A. Bowring, Geophysics and geochronology of the crystalline basement of the Alberta Basin, western Canada, *Can. J. Earth Sci.*, *28*(4), doi:10.1139/e91-045, 1991.

Rost, S., and C. Thomas, Improving seismic resolution through array processing techniques, *Surv. Geophys.*, *30*, 271–299, doi:10.1007/s10712-009-9070-6, 2009.

Russo, R. M., and P. G. Silver, Cordillera formation, mantle dynamics, and the Wilson cycle, *Geology*, *24*(6), 511–514, 1996.

Rychert, C. A., and P. M. Shearer, Resolving crustal thickness using SS waveform stacks, *Geophys. J. Int.*, *180*(3), 1128–1137, doi:10.1111/j.1365-246X.2009.04497.x, 2010.

Sacchi, M. D., Re-weighting strategies in seismic deconvolution, *Geophys. J. Int.*, *129*, 1997.

Sacchi, M. D., and T. J. Ulrych, High resolution velocity gathers and offset space reconstruction, *Geophysics*, *60*, 1995.

Schaeffer, A. J., and M. G. Bostock, A low–velocity zone atop the transition zone in northwestern Canada, *J. Geophys. Res.*, *115* (B06302), doi:10.1029/2009JB006856, 2010.

Schmerr, N., and E. J. Garnero, Upper mantle discontinuity topography from thermal and chemical heterogeneity, *Science*, *318* (5850), 623–626, doi:10.1126/ science.1145962, 2007.

Schmid, C., S. Goes, S. van der Lee, and D. Giardini, Fate of the Cenozoic Farallon slab from a comparison of kinematic thermal modeling with tomographic images, *Earth Planet. Sci. Lett.*, *204* (12), 17–32, doi:10.1016/S0012-821X(02)00985-8, 2002.

Schultz, R., and Y. J. Gu, Flexible, inversion-based MATLAB implementation of the Radon transform, *accepted in Comput. Geosci.*, 2012.

Shearer, P. M., Seismic imaging of upper-mantle structure with new evidence for a 520-km discontinuity, *Nature*, *344*, 121 – 126, doi:10.1038/344121a0, 1990.

Shearer, P. M., Constraints on upper mantle discontinuities from observations of Long-Period reflected and converted phases, *J. Geophys. Res.*, *96* (B11), 18,147–18,182, 1991.

Shearer, P. M., Global mapping of upper mantle reflectors from long-period SS precursors, *Geophys. J. Int*, *115*, 1993.

Shearer, P. M., and G. T. Masters, Global mapping of topography on the 660-km discontinuity, *Nature*, *355*, 1992.

Shearer, P. M., M. P. Flanagan, and M. A. H. Hedlin, Experiments in migration processing of SS precursor data to image upper mantle discontinuity structure, *J. Geophys. Res.*, *104* (B4), 7229–7242, 1999.

Shen, X., H. Zhou, and H. Kawakatsu, Mapping the upper mantle discontinuities beneath China with teleseismic receiver functions, *Earth Planet. Sci. Lett.*, 2008.

Shieh, S. R., H. kwang Mao, R. J. Hemley, and L. C. Ming, Decomposition of phase d in the lower mantle and the fate of dense hydrous silicates in subducting slabs, *Earth Planet. Sci. Lett.*, *159*(1-2), 13–23, doi:10.1016/S0012-821X(98)00062-4, 1998.

Shragge, J., M. G. Bostock, C. G. Bank, and R. M. Ellis, Integrated teleseismic studies of the southern alberta upper mantle, *Can. J. Earth Sci.*, 2002.

Simmons, N. A., A. M. Forte, L. Boschi, and S. P. Grand, GyPSuM: A joint tomographic model of mantle density and seismic wave speeds, *J. Geophys. Res.*, *115*(B12), doi:10.1029/2010JB007631, 2010.

Soudoudi, F., X. Yuan, G. Asch, and R. Kind, High-resolution image of the geometry and thickness of the subducting Nazca lithosphere beneath northern Chile, *J. Geophys. Res.*, *116*(B04302), doi:10.1029/2010JB007829, 2011.

Su, W.-j., R. L. Woodward, and A. M. Dziewoński, Degree 12 model of shear velocity heterogeneity in the mantle, *J. Geophys. Res.*, *99*(B4), 6945–6980, doi: 10.1029/93JB03408, 1995.

Tackley, P. J., D. J. Stevenson, G. A. Glatzmaier, and G. Schubert, Effects of an endothermic phase transition at 670 km depth in a spherical model of convection in the Earth's mantle, *Nature*, *361*, 699–704, doi:10.1038/361699a0, 1993.

Tauzin, B., E. Debayle, and G. Wittlinger, The mantle transition zone as seen by global Pds phases: no clear evidence for a thin transition zone beneath continents, *J. Geophys. Res.*, *113*(B08309), doi:10.1029/2007JB005364, 2008.

Tauzin, B., E. Debayle, and G. Wittlinger, Seismic evidence for a global low-velocity layer within the Earth's upper mantle, *Nature Geosci*, *3*(10), 718–721, doi:10.1038/ngeo969, 2010.

Thompson, D. A., G. Helffrich, I. D. Bastow, J. M. Kendall, J. Wookley, D. W. Eaton, and D. B. Snyder, Implications of a simple mantle transition zone beneath cratonic North America, *Earth Planet. Sci. Lett.*, doi:10.1016/j.epsl.2011.09.037, 2011.

Tikhonov, A. N., *Ill-posed problems in the natural sciences*, Mir Publishers, 1987.

Torii, Y., and S. Yoshioka, Physical conditions producing slab stagnation: constraints of the Clapeyron slope, mantle viscosity, trench retreat, and dip angles, *Tectonophysics*, *445*, 200–209, 2007.

Trickett, S. R., F-xy eigenimage noise suppression, *Geophysics*, *68*(2), 2003.

Tromp, J., D. Komatitsch, and Q. Liu, Spectral–element and adjoint methods in seismology, *Comm. Comp. Phys.*, *3*, 1–32, 2008.

van der Lee, S., and G. Nolet, Upper mantle S velocity structure of North America, *J. Geophys. Res.*, doi:10.1029/97JB01168, 1997.

van der Lee, S., D. James, and P. Silver, Upper-mantle S-velocity structure of central and western South America, *J. Geophys. Res.*, *106*(12), 2001.

van der Meijde, M., F. Marone, D. Giardini, and S. van der Lee, Seismic evidence for water deep in Earth's Upper Mantle, *Science*, *300*, 1556–1558, doi:10.1126/science.1083636, 2003.

van der Meijde, M., S. van der Lee, and D. Giardini, Seismic discontinuities in

the Mediterranean mantle, *Phys. Earth Planet. Int.*, *148*(2-4), 233–250, doi: 10.1016/j.pepi.2004.09.008, 2005.

VanDecar, J. C., D. E. James, and M. Assumpçāo, Seismic evidence for a fossil mantle plume beneath South America and implications for plate driving forces, *Nature*, *378*, 25–31, 1995.

Vinnik, L. P., Detection of waves converted from P to SV in the mantle, *Phys. Earth Planet. Inter.*, *15*, 39–45, 1977.

Wen, L., and D. L. Anderson, Layered mantle convection: A model for geoid and topography, *Earth Planet. Sci. Lett.*, *146*, 367–377, doi:10.1016/S0012-821X(96)00238-5, 1997.

Wölbern, I., B. Heit, X. Yuan, G. Asch, R. Kind, J. Viramonte, S. Tawackoli, and H. Wilke, Receiver function images from the Moho and the slab beneath the Altiplano and Puna plateaus in the Central Andes, *Geophys. J. Int.*, *177*(1), 296–308, doi:10.1111/j.1365-246X.2008.04075.x, 2009.

Yilmaz, Ö., *Seismic data analysis: processing, inversion, and interpretation of seismic data*, 2 ed., Society of Exploration Geophysicists, 2001.

Zhao, D., Seismological structure of the subduction zones and its implication for arc magmatism and dynamics, *Phys. Earth Planet. Inter.*, *127*, 197–214, 2001.

Zheng, Y., T. Lay, M. P. Flanagan, and Q. Williams, Pervasive Seismic Wave Reflectivity and Metasomatism of the Tonga Mantle Wedge, *Science*, *316*(855), doi:10.1126/science.1138074, 2007.

Zheng, Z., and B. Romanowicz, Do double "ss precursors" mean double discontinuities?, *Geophys. J. Int.*, 2012.

Zhou, Y., F. Dahlen, and G. Nolet, Three-dimensional sensitivity kernels for surface wave observables, *Geophys. J. Int.*, *158*, 142–168, 2004.